

## Generalized Mechanistic Framework for Ethane Dehydrogenation and Oxidative Dehydrogenation on Molybdenum Oxide Catalysts

Rui Yao, José E. Herrera, Lihang Chen, and Ya-Huei Cathy Chin\*

Cite This: *ACS Catal.* 2020, 10, 6952–6968

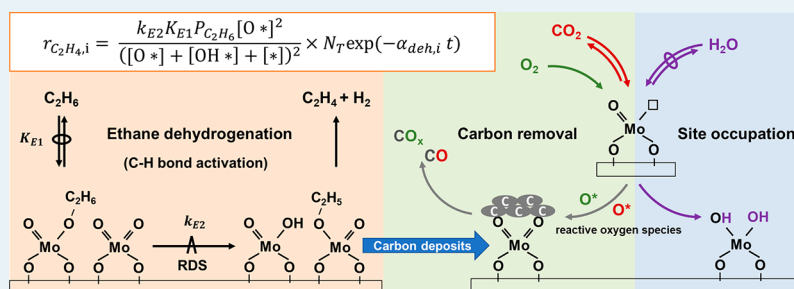
Read Online

ACCESS |

Metrics &amp; More

Article Recommendations

Supporting Information



**ABSTRACT:** Ethane turnovers to ethylene in either oxidative dehydrogenation with diverse oxidants ( $O_2$ ,  $CO_2$ ,  $H_2O$ ) or dehydrogenation (without an oxidant) over two-dimensional  $MoO_x$  dispersed on  $Al_2O_3$  catalyst occur via a generalized mechanistic framework encompassing ternary catalytic cycles of  $C_2H_6$  activation, oxidant activation, and carbon removal. This is confirmed from rate assessments, detailed kinetic analysis accounting for active site loss, isotopic tracer studies, and detailed spectroscopic characterization. Irrespective of the oxidant's chemical identity, the  $C_2H_6$  activation cycle occurs via the kinetically relevant C–H bond activation of  $C_2H_6$  on lattice oxygen of  $MoO_x$ , forming  $C_2H_4$ . The concomitant oxidant activation cycle either replenishes the oxygen vacancies or generates reactive oxygen species, which scavenge unwanted carbonaceous debris deposited on catalyst surfaces at contents dictated by the chemical identity of the oxidant and oxygen chemical potential that it exerts. Among the oxidants,  $O_2$  is the most effective, as it removes coke effectively, leading to essentially no rate decay.  $CO_2$  and  $H_2O$  are alternate soft oxidants, and their use prevents the overoxidation of ethylene, thus resulting in higher ethylene selectivity (80–85%) than using  $O_2$ .  $CO_2$  activation is, however, severely restricted kinetically, as evidenced from the reverse water–gas shift reaction that is far away from chemical equilibrium; thus, the generation of reactive oxygen species and their ability to concomitantly oxidize coke are much less effective than those with  $O_2$  oxidant.  $H_2O$  dissociation is rapid and quasi-equilibrated, but its activation converts a portion of the active lattice oxygen to hydroxy species, reducing the active oxygen centers and lowering  $C_2H_6$  turnovers. The rates of the  $C_2H_6$  activation cycle dictate the intrinsic rates, whereas those of the concomitant oxidant activation and carbon removal cycles dictate the surface lattice oxygen density available for catalysis and in turn the extent of rate decay. Consolidating these findings within a generalized mechanistic framework leads to a universal rate expression containing two terms, one accounting for an intrinsic  $C_2H_6$  activation rate and a second one for the time-dependent rate decay. This universal rate expression captures the kinetic properties of early transition-metal oxides in  $C_2H_6$  catalysis, irrespective of the chemical identity of the oxidant.

**KEYWORDS:** ethane, molybdenum oxide, C–H activation, oxidative dehydrogenation, soft oxidants,  $CO_2$ , deactivation, reverse water–gas shift

## 1. INTRODUCTION

The marked increase in shale gas production has made light alkanes abundant, alternative chemical feedstocks. For this reason, ethane, the second most abundant component (up to 15 vol %) in shale gas,<sup>1</sup> has become an attractive precursor, replacing naphtha for the production of ethylene, a commodity chemical for the synthesis of polyethylene, styrene, ethylene oxide, ethylene glycol, and other value-added compounds.<sup>2</sup> This shift in petrochemical feedstock causes a concomitant shift in ethylene production technology, from steam cracking to dehydrogenation/oxidative dehydrogenation.

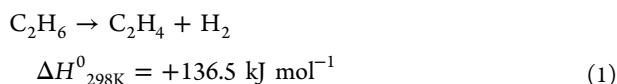
Thermal and catalytic dehydrogenations of ethane are energetically intensive processes and prone to coke deposition.<sup>3,4</sup> The reactions inevitably require high temperature, because of their strong endothermicity, making them limited by equilibrium at the lower temperatures (eq 1).

Received: March 4, 2020

Revised: May 16, 2020

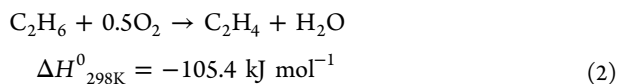
Published: June 10, 2020



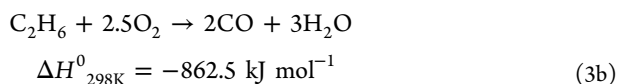
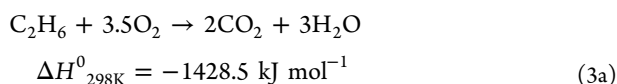


Therefore, managing the energy transport in these heat-intensive processes and suppressing coke formation inside the reactor are the two major challenges, which often limit the reactor operation to low ethane partial pressures and short residence times.<sup>5</sup>

Oxidative dehydrogenation (ODH), which uses O<sub>2</sub> as the coreactant, is an alternative path for ethylene production from ethane.

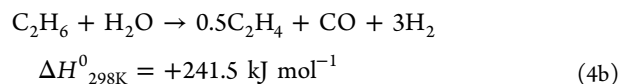
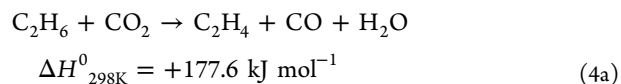


Through this reaction, O<sub>2</sub> combines with the abstracted hydrogen atoms, releasing heat, thus making the overall reaction exothermic and altering the heat requirements such that the process becomes energetically less intensive. A portion of the oxygen, however, reacts with the ethane-derived carbonaceous species, transforming them into CO<sub>x</sub> (eqs 3a and 3b), decreasing the overall selectivity to ethylene.

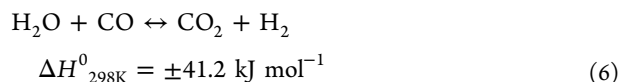
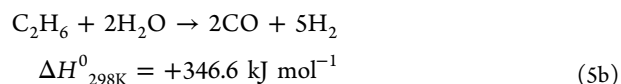
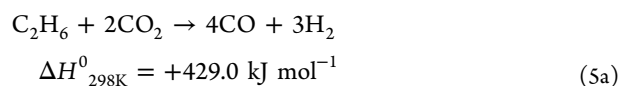


Among various catalysts investigated for ODH processes, the redox-type, dispersed molybdenum oxides are attractive candidates, because their lattice oxygen atoms assist with activating the C–H bonds in light alkane (C<sub>2</sub>–C<sub>3</sub>) via a Mars-van Krevelen mechanism.<sup>6,7</sup> On MoO<sub>x</sub>/Al<sub>2</sub>O<sub>3</sub> catalysts, propane ODH rates (per Mo atom) increase with increasing Mo surface densities and approach a maximum value at ~4.5 Mo·nm<sup>-2</sup>. This observed rate increase appears to reflect an increase in the reactivity of lattice oxygen sites, as the size of MoO<sub>x</sub> domains increases and their footprint attains near monolayer coverages. As the MoO<sub>x</sub> coverages increase to a monolayer, lattice oxygen atoms become more weakly bound and MoO<sub>x</sub> reducibility concomitantly increases.<sup>8</sup> Beyond the monolayer coverage, turnover rate (per Mo atom) decreases, as large, bulk crystalline MoO<sub>3</sub> structures form and a portion of the molybdenum (and the associated oxygen) becomes inaccessible to the alkane reactant for catalysis. Similar volcano type dependence between turnover rates and MoO<sub>x</sub> surface densities was also reported for ethane ODH, where two-dimensional molybdenum species with their Mo ions fully dispersed on alumina surface are most reactive.<sup>9,10</sup> Previous studies have proposed that the Mo=O bond strength correlates directly to its alkane ODH reactivity, because the weakly bound lattice oxygen is more effective than those strongly bound ones in abstracting the leaving hydrogen during the kinetically relevant C–H bond activation of alkanes, thus leading to a higher reactivity.<sup>11</sup> This mechanistic understanding is consistent with the reactivity trends when incorporating alkali (Cs, K, Li) dopants into the catalysts—alkali oxides can decrease the reducibility of MoO<sub>x</sub>, strengthen the Mo=O bond, and in turn inhibit ODH reaction, as found for propane ODH on alkali doped MoO<sub>x</sub>/ZrO<sub>2</sub> catalysts.<sup>12</sup>

Besides conventional ODH, which uses O<sub>2</sub> as the coreactant, ODH can also occur when using CO<sub>2</sub> and H<sub>2</sub>O as alternative oxidants:



CO<sub>2</sub> and H<sub>2</sub>O are attractive alternatives to O<sub>2</sub>, because they are considered as “soft oxidants”; that is, they would not undergo total combustion reactions with ethane and ethylene. By eliminating the total combustion routes, their use preserves the overall carbon atom efficiency and can potentially enhance the selectivity to ethylene. The use of CO<sub>2</sub> and H<sub>2</sub>O co-oxidants, however, promotes parallel dry reforming (eq 5a) and steam reforming (eq 5b) processes, together with the forward/reverse water–gas shift reactions (eq 6).



These additional pathways, which either produce syngas or shuffle CO<sub>2</sub>–CO (or the related H<sub>2</sub>O–H<sub>2</sub>), have further complicated rate data analyses, making the kinetic assessments and rate data interpretation difficult.

Previous studies have established that molybdenum-based catalysts (Mo<sub>2</sub>C) exhibit exceptional selectivity to ethylene during ethane ODH with CO<sub>2</sub>.<sup>13,14</sup> During C<sub>2</sub>H<sub>6</sub>–CO<sub>2</sub> catalysis, Mo oxide moieties on Mo<sub>2</sub>C activate ethane, preserving its C–C bond and at the same time retarding coke formation.<sup>14</sup> Incorporating Fe can stabilize MoO<sub>x</sub> effectively and enhance ethylene yield and catalyst stability.<sup>14</sup> Other late transition-metal catalysts such as Pt,<sup>13</sup> Co,<sup>15</sup> and Ni<sup>15</sup> are effective catalysts for activating alkanes, but these catalysts, unlike MoO<sub>x</sub>, are also reactive in cleaving the C–C bond via the undesired reforming reactions, producing CO<sub>x</sub> side products.

A detailed mechanism for ethane ODH with O<sub>2</sub>, CO<sub>2</sub>, or H<sub>2</sub>O co-oxidants over molybdenum oxide catalysts that includes carbon deposition and removal events has not yet been established. Here, we describe the mechanistic similarities and differences for ethane ODH using these diverse oxidants on dispersed molybdenum oxide catalysts through a rigorous kinetic assessment and characterization of the catalysts, upon their contact with various reaction mixtures. Ethane oxidative dehydrogenation catalysis follows three kinetically coupled cycles, namely, the initial activation of the C–H bond of ethane, the activation of O<sub>2</sub>, CO<sub>2</sub>, or H<sub>2</sub>O (which replenishes the oxygen vacancies or generates reactive oxygen species), and the coke formation and oxidation from catalyst surfaces. These common mechanistic elements with similar kinetically coupled catalytic cycles lead to a general rate expression capturing the reactivities for the different catalytic systems. The rate expression accurately describes the intrinsic rates as well as secondary time-dependent

deactivation events. The intrinsic ethane turnover rates are largely insensitive to the chemical identity of the co-oxidant, in contrast to the time-dependent deactivation profiles, as the latter is largely dictated by the ability of the co-oxidant to oxidize and remove surface carbonaceous deposits.

## 2. EXPERIMENTAL METHODS

**2.1. Synthesis of Molybdenum Oxide Catalysts.**  $\text{Al}_2\text{O}_3$ -supported molybdenum oxide catalysts were prepared by an incipient wetness impregnation method. The  $\text{Al}_2\text{O}_3$  particles (Sasol, Puralox TH 100/150,  $0.96 \text{ cm}^3 \text{ g}^{-1}$  pore volume,  $150 \text{ m}^2 \text{ g}^{-1}$  surface area, less than  $75 \mu\text{m}$  particle diameter) were first heated in stagnant air to 1023 at  $0.083 \text{ K s}^{-1}$  and then isothermally held for 8 h before being cooled to 393 K. The treated  $\text{Al}_2\text{O}_3$  particles were impregnated with an ammonium molybdate solution, prepared by dissolving  $(\text{NH}_4)_6\text{Mo}_7\text{O}_{24} \cdot 4\text{H}_2\text{O}$  (Sigma-Aldrich, ACS reagent, 99.98% trace metals basis) precursor in deionized water ( $>18.2 \text{ M}\Omega \text{ cm}$ ) at the concentration needed to achieve a molybdenum oxide loading of either 13.5 or 25 wt %.  $\text{SiO}_2$ -supported 13.5 wt % molybdenum oxide catalyst was prepared using a similar procedure, except that silica gel (Sigma-Aldrich, high-purity grade,  $1.15 \text{ cm}^3 \text{ g}^{-1}$  pore volume,  $300 \text{ m}^2 \text{ g}^{-1}$  surface area,  $35\text{--}75 \mu\text{m}$  particle diameter) was used as the support. After impregnation, the samples were aged at ambient conditions for 12 h and then dried at 393 K for 12 h in stagnant air. Following this stage, samples were treated in flowing dry air (Linde, 99.99%,  $0.33 \text{ cm}^3 \text{ g}_{\text{cat}}^{-1} \text{ s}^{-1}$ ) by being heated at  $0.033 \text{ K s}^{-1}$  to 873 K and held isothermally at 873 K for 4 h, before being cooled to ambient temperature. Crystalline  $\text{MoO}_3$  catalyst was prepared by treating the solid  $(\text{NH}_4)_6\text{Mo}_7\text{O}_{24} \cdot 4\text{H}_2\text{O}$  precursor following the same heating procedure.

**2.2. Catalytic Tests and Isotopic Measurements.** The catalyst powders ( $<75 \mu\text{m}$ ) were pressed into pellets using a pellet die (Carver, 31 mm i.d.) at 130 MPa for 20 min in a hydraulic press (Specac). The resulting pellets were then sieved to obtain agglomerates between 125 and 180  $\mu\text{m}$ . These agglomerates were held on a quartz supporting frit to form a packed catalyst bed within a tubular microcatalytic plug flow reactor (quartz, 8.1 mm i.d.) equipped with a K-type thermocouple placed at the center (in both axial and radial directions) of the packed bed. Prior to rate measurements, the catalyst samples were pretreated in situ under  $1.67 \text{ cm}^3 \text{ g}^{-1} \text{ s}^{-1}$  flowing Ar (Linde, 99.999%) at a ramp rate of  $0.05 \text{ K s}^{-1}$  to 873 K before exposure to reactants. Reactant mixtures were prepared by metering  $\text{C}_2\text{H}_6$  (Linde certified standard, 20.0%  $\text{C}_2\text{H}_6$  in Ar),  $\text{CO}_2$  (Linde, 99.99%),  $\text{O}_2$  (Linde certified standard, 5.0%  $\text{O}_2$  in Ar), and balanced Ar (Linde, 99.999%) independently with thermal mass-flow controllers (Brooks, SLA5850). Water vapor was introduced by evaporating liquid water (doubly deionized,  $>18.2 \text{ M}\Omega \text{ cm}$ ) into a vaporization zone, which was held isothermally at 383 K, through a syringe (1  $\text{cm}^3$ , Hamilton) mounted on a syringe infusion pump (KD Scientific, LEGATO 100), and then mixed with upstream reactant mixtures. All transfer gas lines were heated and held at 383 K after water was introduced to prevent its condensation. Chemical compositions of the effluent streams ( $\text{CO}$ ,  $\text{H}_2$ ,  $\text{CH}_4$ ,  $\text{CO}_2$ ,  $\text{C}_2\text{H}_4$ , and  $\text{C}_2\text{H}_6$ ) were quantified by a micro gas chromatograph (Varian CP-4900) equipped with HP-PLOT U and Mol Sieve 5A columns, connected to a thermal conductivity detector (TCD). Before it entered the micro gas chromatograph, water was removed from the reactor effluent stream by a water trap packed with drying

agent (Drierite, Sigma-Aldrich, 98%  $\text{CaSO}_4$  and 2%  $\text{CoCl}_2$ , 8 mesh).

Transient experiments were performed using  $\text{C}_2\text{H}_6$  mixtures (without an oxidant, balanced with Ar) in the plug flow reactor system described above. Concentrations of  $\text{H}_2$  and  $\text{H}_2\text{O}$  present in the effluent stream were quantified in an online mass spectrometer (Pfeiffer OmniStar) using Ar as the internal standard. Concentrations of  $\text{CO}$ ,  $\text{CH}_4$ ,  $\text{C}_2\text{H}_4$ , and  $\text{C}_2\text{H}_6$  in the effluent stream were determined using a micro gas chromatograph (Varian CP-4900).

Isotopic exchange studies were performed with  $\text{H}_2\text{-D}_2$  (99.999%  $\text{H}_2$ , Linde; 99.995%  $\text{D}_2$ , Linde) and  $\text{H}_2\text{-D}_2\text{O}$  (99.999%  $\text{H}_2$ , Linde; 99.9 atom % D in  $\text{D}_2\text{O}$ , Sigma-Aldrich) mixtures using the same plug flow reactor system. Concentrations of isotopomers, that is,  $\text{H}_2$ , HD,  $\text{D}_2$ ,  $\text{H}_2\text{O}$ , HDO, and  $\text{D}_2\text{O}$  in the effluent streams, were determined by an online mass spectrometer (Pfeiffer OmniStar), in which Ar was used as the internal standard.

**2.3. Catalyst Characterization.** Powder X-ray diffraction (XRD) patterns were recorded on a Rigaku Miniflex 600 diffractometer with  $\text{Cu K}\alpha$  ( $\lambda = 1.789 \text{ \AA}$ ) radiation opening at 35 kV and 40 mA. A  $2\theta$  scan range from  $10^\circ$  to  $80^\circ$  with a step size of  $0.02^\circ$  and a scan speed of  $0.5 \text{ s/step}$  were used for the analysis.

Raman spectra were collected using a custom-made Raman instrument equipped with an imaging spectrograph (Spectro-Pro-2500i, Acton Research Corporation) and a liquid-nitrogen-cooled charge coupled device (CCD) detector (Acton). The visible excitation at 532 nm was supplied by a diode-pumped solid-state (DPSS) laser with a power of  $\sim 2.0 \text{ mW}$  at sample position. A spectral resolution of less than  $0.5 \text{ cm}^{-1}$  was achieved by using a 1200 lines/mm grating. The Raman shift was calibrated by interpolation of the Rayleigh line and a silicon wafer signal ( $520 \text{ cm}^{-1}$ ). The main peak heights were used to determine the D-to-G band intensity ratios ( $I_D/I_G$ ). This methodology was selected, as opposed to using the area ratios, to avoid arbitrary assignment of the limits for the integral function and the associated statistically larger standard deviations, as found and reported previously.<sup>16</sup> A localized Gaussian peak-fitting methodology using Origin software was utilized to find both the absolute heights and wavenumber positions of D and G bands.

High-resolution X-ray photoelectron spectroscopy (XPS) was performed with a Thermo Scientific ESCALAB 250Xi photoelectron spectrometer (E. Grinstead) equipped with a monochromatic Al  $\text{K}\alpha$  source (900  $\mu\text{m}$ ) and a sample preparation chamber under 101 kPa Ar controlled to less than 1 ppm of  $\text{O}_2$ . The fresh catalyst sample (sample *fresh*) was directly transferred into the sample preparation chamber without further treatment. The spent catalyst samples were prepared by first pelletizing the fresh powder samples into a self-supporting wafer (5 mm diameter), loading the pellets into a stainless steel plug flow reactor (7 mm i.d.) equipped with two isolation valves, and then treating it with a mixture containing 5 kPa  $\text{C}_2\text{H}_6$  and either 3.2 kPa  $\text{O}_2$  (sample *spent O<sub>2</sub>*),  $\text{CO}_2$  (sample *spent CO<sub>2</sub>*), or  $\text{H}_2\text{O}$  (sample *spent H<sub>2</sub>O*) or with 5 kPa  $\text{C}_2\text{H}_6$  (without an oxidant, sample *spent no*), balanced in Ar, for 15 h at 873 K. After the above treatment, the samples were purged with flowing Ar for 12 h isothermally before being cooled to ambient temperature and subsequently isolated by closing off the valves at both reactor inlet and outlet, prior to transferring to the sample preparation chamber. Under the controlled environment of the sample preparation chamber, the sample was loaded onto a sample holder carousel and then

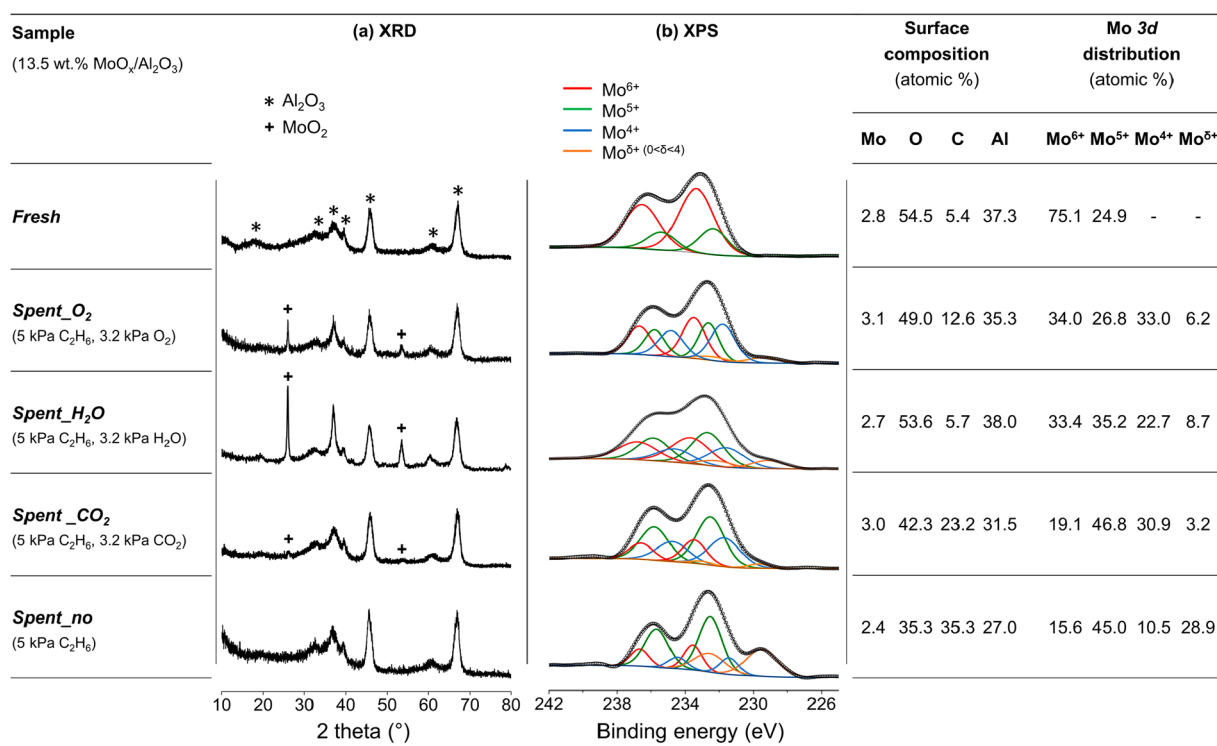


**Figure 1.** (a) XRD patterns and (b) Mo 3d XPS spectra, together with the distribution of surface atomic composition and Mo chemical states, on 13.5 wt % MoO<sub>x</sub>/Al<sub>2</sub>O<sub>3</sub> catalysts before and after C<sub>2</sub>H<sub>6</sub> reactions with various oxidants (O<sub>2</sub>, H<sub>2</sub>O, CO<sub>2</sub>) and without an oxidant for 15 h at 873 K (6000 cm<sup>3</sup> h<sup>-1</sup> g<sub>cat</sub><sup>-1</sup>).

transferred into the ultrahigh vacuum (UHV) compartment of the spectrometer for XPS analysis. The vacuum pressure in the analysis chamber was  $\sim 2 \times 10^{-9}$  Torr, and the charge compensation was performed using an e<sup>-</sup>/Ar<sup>+</sup> flood gun. Spectrum deconvolution was performed using Avantage and Origin software with all electron binding energies referred to the C 1s (adventitious carbon) peak at 284.5 eV. The spectra were analyzed using a Shirley background subtraction followed by deconvolution using mixed Gaussian–Lorentzian functions (70%–30%). The distance of the two spin–orbit coupling components of Mo, that is, Mo 3d<sub>5/2</sub> and Mo 3d<sub>3/2</sub>, was fixed at 3.1 eV with a peak area ratio of 3:2.<sup>17</sup> The Mo 3d<sub>5/2</sub> spectra were deconvoluted, by assigning the Mo<sup>6+</sup> at 233.6 eV, Mo<sup>5+</sup> at 232.6 eV, Mo<sup>4+</sup> at 231.6 eV, and Mo<sup>δ+</sup> (0 < δ < 4) at 229.5 eV, with their full width at half-maximum (fwhm) of 1.7, 1.8, 1.7, and 2.2 eV, respectively, following previously established methodology.<sup>17,18</sup> The C 1s spectra were fitted using contributions from O=C=O at 288.4 eV, C–O at 285.2 eV, C–C at 284.1 eV, and carbide (C–Mo) at 283.2 eV, with their fwhm of 3.4, 1.6, 1.5, and 1.0 eV, respectively, following again methodology available in the literature.<sup>17</sup> The binding energy values contain a  $\pm 0.15$  eV error, and the fwhm values have a  $\pm 0.2$  eV error.

Diffuse reflectance UV–vis spectroscopy studies were performed in a Praying Mantis (Harrick Scientific) DRS cell mounted onto a Shimadzu UV–vis 3600 spectrophotometer. The optical absorption data were obtained using a tungsten lamp (visible range, cut off at 360 nm) and a deuterium lamp (range of 360–190 nm). The UV–vis spectra were referenced to a Spectralon standard (DRP-SPR, Harrick Scientific). The acquired diffuse reflectance spectra were converted into the Kubelka–Munk function  $[F(R_{\infty})]$ .<sup>19</sup> The absorption edge energies were determined using Tauc’s law following Davis and Mott’s methodology,<sup>20</sup> defined as the  $\alpha$ -intercept of the

straight line describing the near-edge region of the spectra, plotted in  $[F(R_{\infty}) \cdot h\nu]^{1/2}$  as a function of the energy of the incident photon,  $h\nu$ , with the assumption of an indirect optical transition formalism.

Temperature-programmed oxidation (TPO) measurements were performed using the microcatalytic plug flow reactor system described above. For this purpose, 20 mg of spent catalysts was placed into the reactor. The samples were heated at 5 K min<sup>-1</sup> from ambient temperature to 1023 K in 1.1 kPa O<sub>2</sub> at 90 cm<sup>3</sup> min<sup>-1</sup> (5.0% O<sub>2</sub>/He, Linde certified standard; He, Linde, 99.999%), during which all the carbon converted to CO<sub>2</sub> (C + O<sub>2</sub> → CO<sub>2</sub>). The CO<sub>2</sub> evolution profiles were quantified using a methanator-FID setup (FID = flame ionization detector). The methanator, which contains a Ni/Al<sub>2</sub>O<sub>3</sub> catalyst, converted all the evolved CO<sub>2</sub> into CH<sub>4</sub> for sequential quantification using an FID detector. After each experiment, the FID detector was calibrated with pulses of CO<sub>2</sub> ( $\sim 11.16$  μmol), controlled by a six-way valve (13T-0345 V, Valco Instrument). The cumulative amount of CO<sub>2</sub> is related to the amount of carbon on the catalyst, which was then expressed as C/Mo atomic ratio. The deconvolution of the TPO profiles into multiple peaks was performed by fitting the TPO profiles with Gaussian-type functions using Origin software. The shift in the maximum temperature of the peaks was within  $\pm 10$  K.

### 3. RESULTS AND DISCUSSION

#### 3.1. Chemical State, Size, and Structure of MoO<sub>x</sub> Domains in the Fresh 13.5 wt % MoO<sub>x</sub>/Al<sub>2</sub>O<sub>3</sub> Catalyst.

The XRD pattern for the fresh 13.5 wt % MoO<sub>x</sub>/Al<sub>2</sub>O<sub>3</sub> catalyst (Figure 1a, sample *fresh*) shows the characteristic diffractions of  $\gamma$ -Al<sub>2</sub>O<sub>3</sub> (19.35°, 31.86°, 37.55°, 39.28°, 45.68°, 60.56°, and 66.58°) but not those of crystalline MoO<sub>3</sub> (23.7°, 25.8°, and

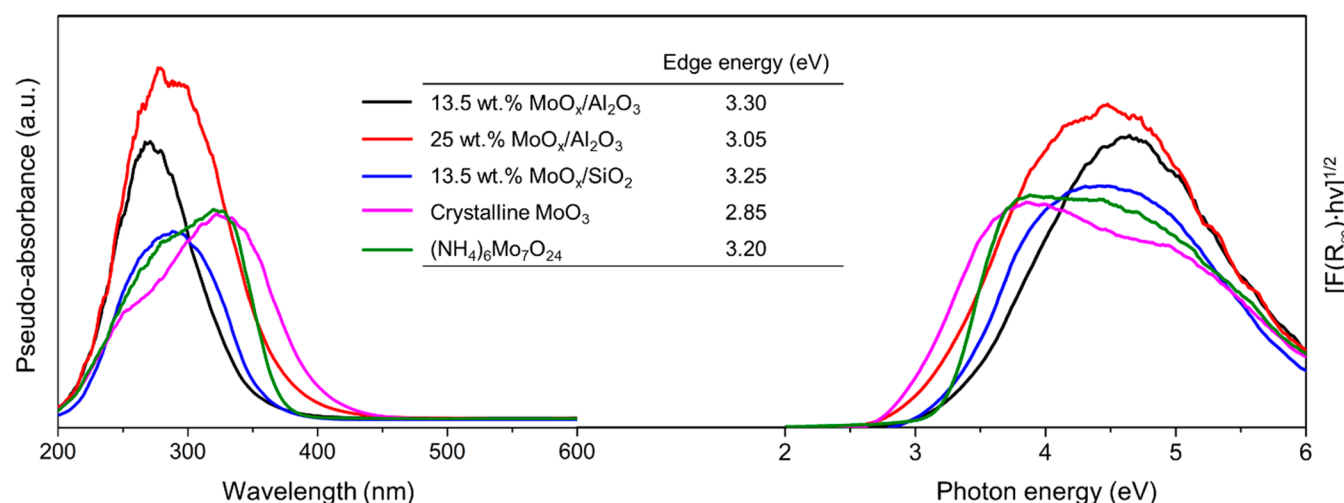


**Figure 2.** UV–Vis diffuse reflectance spectra (left) and Tauc plots (right) of 13.5 wt % MoO<sub>x</sub>/Al<sub>2</sub>O<sub>3</sub>, 25 wt % MoO<sub>x</sub>/Al<sub>2</sub>O<sub>3</sub>, and 13.5 wt % MoO<sub>x</sub>/SiO<sub>2</sub>. Spectra of crystalline MoO<sub>3</sub> and (NH<sub>4</sub>)<sub>6</sub>Mo<sub>7</sub>O<sub>24</sub> are included as references.

27.4°), indicating that Mo is well-dispersed, likely as two-dimensional moieties or three-dimensional nanoparticles with an average domain size below 4 nm.<sup>21</sup> Raman spectroscopy was used to reveal molecular-level information on the MoO<sub>x</sub> structure and its degree of oligomerization.<sup>22</sup> The Raman spectrum of the fresh catalyst (Figure S1) shows a major band centered at 950 cm<sup>-1</sup>, previously assigned to the symmetric stretching of the terminal Mo=O bond of two-dimensional MoO<sub>x</sub> oligomers dispersed on alumina.<sup>8,23</sup> The broad bands at 830 and 580 cm<sup>-1</sup> are associated with the asymmetric and symmetric vibrations of bridging Mo–O–Mo bonds in the oligomers, respectively.<sup>24,25</sup> The weak bands observed at 220 and 360 cm<sup>-1</sup> are related to the bending modes of the same species.<sup>25</sup> In addition, there is a small shoulder that appeared at ~1000 cm<sup>-1</sup>, likely arising from the Mo=O stretching of crystalline MoO<sub>3</sub> structures.<sup>8,26–28</sup> However, this small shoulder is not the main feature of the spectra, which suggests that the amount of crystalline MoO<sub>3</sub> is very small, consistent with the absence of clearly defined MoO<sub>3</sub> diffraction features in XRD. These results indicate that two-dimensional structures exist dominantly on the alumina surface, even at 13.5 wt % MoO<sub>x</sub> loading.

Figure 1b shows the high-resolution XPS spectrum in the Mo 3d region for the 13.5 wt % MoO<sub>x</sub>/Al<sub>2</sub>O<sub>3</sub> catalyst and the corresponding fitting result of the same sample (sample fresh). Spectrum deconvolution reveals the Mo 3d<sub>5/2</sub> signals at 233.6 and 232.6 eV; the former is assigned to the Mo<sup>6+</sup> species,<sup>29</sup> corresponding well to the reported range of 233.2–233.8 eV, and the latter is assigned to the Mo<sup>5+</sup> species.<sup>30</sup> The presence of the Mo<sup>5+</sup> (24.9%) might be an indication of the highly dispersed nature of the molybdenum oxide, as previous reports<sup>9,31,32</sup> indicate that, at lower Mo loadings, the binding energy of Mo becomes smaller than that observed on samples with higher loadings and bulk MoO<sub>3</sub>. The other possibility is the existence of either absorbed water or OH groups on MoO<sub>x</sub> domains, which could cause a shift in the Mo 3d<sub>5/2</sub> binding energies to lower values, as previously reported.<sup>33,34</sup> Additionally, the surface atomic fraction of Mo is 2.8%, while the surface atomic ratio of Mo/Al is 0.075. These measured values, when compared to the bulk atomic fraction of 2.1% and the related Mo/Al atomic ratio of 0.055 (calculated by assuming 13.5 wt % of catalyst is bulk MoO<sub>3</sub> and 86.5 wt % of that is Al<sub>2</sub>O<sub>3</sub> in a well-mixed phase),

confirm that the molybdenum species are highly dispersed on the Al<sub>2</sub>O<sub>3</sub> surface.

UV–Visible absorption spectroscopy probes the ligand to metal charge transfer band (LMCT) of molybdenum oxide and correlates it to coordination environment and degree of oligomerization.<sup>11,35,36</sup> Figure 2 (left) shows the UV–vis spectrum of the 13.5 wt % MoO<sub>x</sub>/Al<sub>2</sub>O<sub>3</sub>, together with those of a higher loading of 25 wt % MoO<sub>x</sub>/Al<sub>2</sub>O<sub>3</sub>, reference 13.5 wt % MoO<sub>x</sub>/SiO<sub>2</sub>, crystalline MoO<sub>3</sub>, and (NH<sub>4</sub>)<sub>6</sub>Mo<sub>7</sub>O<sub>24</sub> samples. The absorption maxima observed for the 13.5 wt % MoO<sub>x</sub>/Al<sub>2</sub>O<sub>3</sub> sample appears at ~270 nm, while those of 13.5 wt % MoO<sub>x</sub>/SiO<sub>2</sub> and 25 wt % MoO<sub>x</sub>/Al<sub>2</sub>O<sub>3</sub> sit at 290 and 285 nm, respectively. Absorption bands centered at 230–260 nm are characteristic of isolated tetrahedral molybdate species, while a band at 280 nm can be ascribed to monomers, dimers, or polymerized molybdate species in an octahedral environment.<sup>37</sup> The surface of the 13.5 wt % MoO<sub>x</sub>/Al<sub>2</sub>O<sub>3</sub> catalyst is probably covered by diverse monomeric, dimeric, and polymerized octahedral molybdate species, while more aggregated Mo species are observed at a higher loading (25 wt % MoO<sub>x</sub>/Al<sub>2</sub>O<sub>3</sub>) or when the interaction between Mo species and the support is weaker (as in the case of the 13.5 wt % MoO<sub>x</sub>/SiO<sub>2</sub> sample). For the bulk MoO<sub>3</sub> sample, which consists of infinite distorted octahedral MoO<sub>6</sub> units, the absorption maxima is observed at ~330 nm due to electronic delocalization through Mo–O–Mo bridges.<sup>24,37</sup> For the (NH<sub>4</sub>)<sub>6</sub>Mo<sub>7</sub>O<sub>24</sub> compound, oligomeric distorted MoO<sub>6</sub> units result in an LMCT absorption band at ~320 nm. Linear extrapolation of the absorption edge of the UV–vis diffuse reflectance spectra, using an indirect allowed transition formalism, provides the electron transition energies for the molybdenum moieties in the catalyst.<sup>35,38,39</sup> The absorption edge energy for 13.5 wt % MoO<sub>x</sub>/Al<sub>2</sub>O<sub>3</sub>, derived from the spectrum in Figure 2 (right), is ~3.3 eV, which is very close to that reported for a polymolybdate monolayer.<sup>8</sup> The 13.5 wt % MoO<sub>x</sub>/SiO<sub>2</sub> and 25 wt % MoO<sub>x</sub>/Al<sub>2</sub>O<sub>3</sub> samples exhibit lower adsorption edge energies (3.25 and 3.05 eV, respectively), as a result of a larger degree of metal oxide oligomerization. For crystalline MoO<sub>3</sub> reference sample, the edge energy value obtained is found at 2.85 eV, consistent with the delocalization of the electronic state through the bulk, continuous MoO<sub>3</sub> lattice. The results clearly indicate that the molybdenum oxides in the 13.5 wt % MoO<sub>x</sub>/Al<sub>2</sub>O<sub>3</sub> catalyst are very well-dispersed.

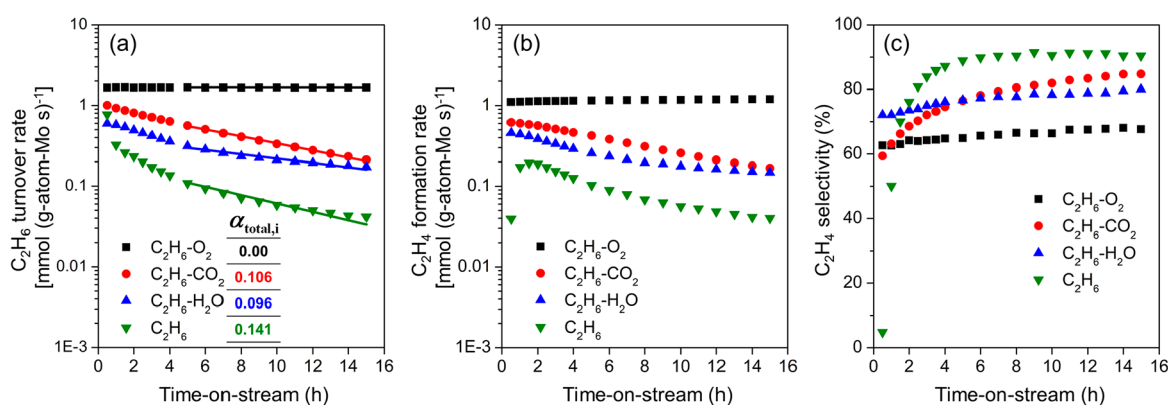


**Figure 3.** Time-dependent catalytic performance during C<sub>2</sub>H<sub>6</sub>-O<sub>2</sub>, C<sub>2</sub>H<sub>6</sub>-H<sub>2</sub>O, C<sub>2</sub>H<sub>6</sub>-CO<sub>2</sub>, and C<sub>2</sub>H<sub>6</sub> reactions on 13.5 wt % MoO<sub>x</sub>/Al<sub>2</sub>O<sub>3</sub> catalyst at 873 K: (a) ethane turnover rate (per total Mo atom, the solid lines are the predicted rate profiles by fitting the measured rate data after 4 h of reaction to eq 15), (b) ethylene formation rate (per total Mo atom), (c) ethylene selectivity (reaction condition: 5 kPa C<sub>2</sub>H<sub>6</sub> with 3.2 kPa O<sub>2</sub>, CO<sub>2</sub>, or H<sub>2</sub>O or, alternatively, without any oxidant, 6000 cm<sup>3</sup> h<sup>-1</sup> g<sub>cat</sub><sup>-1</sup>).

**3.2. Oxidant Chemical Identity Effect on Turnover Rates, Selectivity, and Catalyst Stability during C<sub>2</sub>H<sub>6</sub> Catalysis.** Catalytic rates and selectivities during ethane reactions with O<sub>2</sub>, CO<sub>2</sub>, or H<sub>2</sub>O oxidant on the 13.5 wt % MoO<sub>x</sub>/Al<sub>2</sub>O<sub>3</sub> catalyst were evaluated and compared with those obtained in the absence of an oxidant. Depending on whether an oxidant is used and its chemical identity, multiple reactions (eqs 1–6), that is, oxidative dehydrogenation, direct dehydrogenation, combustion, dry reforming, steam reforming, forward/reverse water–gas shift, hydrogenolysis, and carbon deposition may concomitantly occur. The selectivities toward species *j* (*S<sub>j</sub>*, *j* = C<sub>2</sub>H<sub>4</sub>, CO, CO<sub>2</sub>, and CH<sub>4</sub>) are defined, per carbon basis, as the fraction of ethane converted to *j* (eq 7)

$$S_j = \frac{r_j}{\sum r_j} \quad (7)$$

where *r<sub>j</sub>* is the net C<sub>2</sub>H<sub>6</sub> turnover rate (per total Mo atom) for product *j* formation. Figure 3a–c shows the time-dependent C<sub>2</sub>H<sub>6</sub> turnover rates, ethylene formation rates, and ethylene selectivities during these reactions, respectively; Table S1 summarizes the detailed carbon selectivities at different time-on-streams.

The C<sub>2</sub>H<sub>6</sub>-O<sub>2</sub> system forms predominantly C<sub>2</sub>H<sub>4</sub> (~65% selectivity) with undetectable deactivation. Side reactions include hydrogenolysis, which cleaves the C–C bond of C<sub>2</sub>H<sub>x</sub> intermediates, followed by their partial or total oxidation, producing CO<sub>x</sub> and a very small amount of CH<sub>4</sub> (<1.5% selectivity). In the contrasting cases of the C<sub>2</sub>H<sub>6</sub>-CO<sub>2</sub> and C<sub>2</sub>H<sub>6</sub>-H<sub>2</sub>O reaction systems, C<sub>2</sub>H<sub>6</sub> conversion rates were lower than those observed in the C<sub>2</sub>H<sub>6</sub>-O<sub>2</sub> reaction system. When the rates are compared at a fixed time-on-stream (0.5 h), the rates for C<sub>2</sub>H<sub>6</sub> reactions with CO<sub>2</sub> or H<sub>2</sub>O were 2–3 times lower than those obtained using O<sub>2</sub> oxidant. After 8 h, these rates decreased further by nearly an order of magnitude. However, the C<sub>2</sub>H<sub>6</sub> reaction with CO<sub>2</sub> or H<sub>2</sub>O formed C<sub>2</sub>H<sub>4</sub> at much higher selectivities than with O<sub>2</sub>, reaching 77–85% after 4 h, as shown in Figure 3c. This higher selectivity is expected, since total combustion cannot occur with these soft oxidants, while side reactions such as ethane reforming (eqs 5a and 5b) and hydrogenolysis could occur, leading to the formation of CO and additional H<sub>2</sub> and CH<sub>4</sub> as the side products, but at relatively low rates compared to that of ethylene formation, thus maintaining the high carbon selectivity. Additionally, secondary water–gas

shift reactions (eq 6, in both directions) that interconvert CO<sub>2</sub>–CO and H<sub>2</sub>O–H<sub>2</sub> also occur, as these reactions are a part of the catalytic routes of CO<sub>2</sub> and H<sub>2</sub>O activation.

During the C<sub>2</sub>H<sub>6</sub>-CO<sub>2</sub> and C<sub>2</sub>H<sub>6</sub>-H<sub>2</sub>O reactions, the water–gas shift reaction may occur in either the forward or reverse direction, depending on the feed compositions. During C<sub>2</sub>H<sub>6</sub>-CO<sub>2</sub> catalysis, the reverse water–gas shift reaction (RWGS) occurs, and its approach-to-equilibrium ( $\eta_{RWGS}$ ) is defined by the ratio of reaction quotient (*Q<sub>RWGS</sub>*) to its equilibrium constant (*K<sub>RWGS</sub>*).

$$\eta_{RWGS} = \frac{Q_{RWGS}}{K_{RWGS}} = \frac{[P_{CO}][P_{H_2O}]}{[P_{CO_2}][P_{H_2}]} \times \frac{1}{K_{RWGS}} \quad (8a)$$

$\eta_{RWGS}$  values range from 0.08 to 0.18 during 15 h of reaction (5 kPa C<sub>2</sub>H<sub>6</sub>, 3.2 kPa CO<sub>2</sub>, 873 K, 6000 cm<sup>3</sup> h<sup>-1</sup> g<sub>cat</sub><sup>-1</sup>). During C<sub>2</sub>H<sub>6</sub>-H<sub>2</sub>O catalysis, the forward water–gas shift reaction (WGS) occurs, as the feed mixture contains excess water with chemical compositions residing at the opposite side of the equilibrium position. The approach-to-equilibrium ( $\eta_{WGS}$ ) is defined similarly as

$$\eta_{WGS} = \frac{Q_{WGS}}{K_{WGS}} = \frac{[P_{CO_2}][P_{H_2}]}{[P_{CO}][P_{H_2O}]} \times \frac{1}{K_{WGS}} \quad (8b)$$

where *Q<sub>WGS</sub>* and *K<sub>WGS</sub>* are the reaction quotient and equilibrium constant for the forward water–gas shift reaction, respectively.  $\eta_{WGS}$  values remain below 0.08 during 15 h of reaction (5 kPa C<sub>2</sub>H<sub>6</sub>, 3.2 kPa H<sub>2</sub>O, 873 K, 6000 cm<sup>3</sup> h<sup>-1</sup> g<sub>cat</sub><sup>-1</sup>). These approach-to-equilibrium values  $\eta_{RWGS}$  and  $\eta_{WGS}$ , which are far away from unity, confirm that the water–gas shift reactions are not equilibrated; thus, activation of either CO<sub>2</sub> or H<sub>2</sub>O, or both, is kinetically restricted.

Lastly, the rates of direct C<sub>2</sub>H<sub>6</sub> dehydrogenation, in the absence of an oxidant, decrease rapidly during the first hour, exhibiting the lowest conversions among the four catalytic systems. However, its ethylene selectivity is the highest, reaching 90% after 15 h of reaction.

The selectivity to CH<sub>4</sub> remains small (<7% for all cases), and therefore hydrogenolysis is not a dominant reaction path. The selectivities for all products (i.e., C<sub>2</sub>H<sub>4</sub>, CO<sub>2</sub>, or CO) reached constant values within a 4 h period for C<sub>2</sub>H<sub>6</sub> dehydrogenation and C<sub>2</sub>H<sub>6</sub>-H<sub>2</sub>O reactions and within a much shorter time scale for C<sub>2</sub>H<sub>6</sub>-CO<sub>2</sub> and C<sub>2</sub>H<sub>6</sub>-O<sub>2</sub> reactions. During the initial

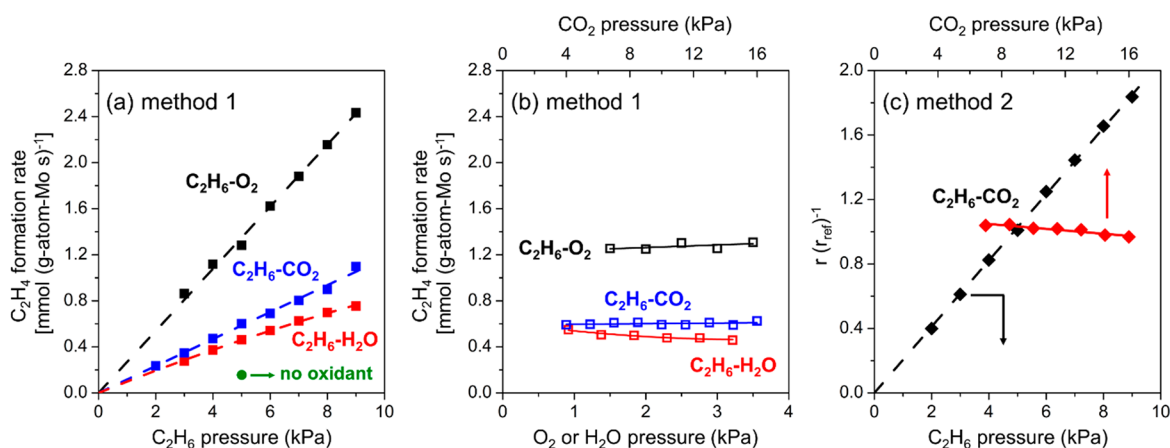


**Figure 4.** Dependences of initial C<sub>2</sub>H<sub>4</sub> formation rate (per total Mo atom) on (a) C<sub>2</sub>H<sub>6</sub> pressure in C<sub>2</sub>H<sub>6</sub>-O<sub>2</sub> (3–9 kPa C<sub>2</sub>H<sub>6</sub> and 3.2 kPa O<sub>2</sub>), C<sub>2</sub>H<sub>6</sub>-H<sub>2</sub>O (3–9 kPa C<sub>2</sub>H<sub>6</sub> and 3.2 kPa H<sub>2</sub>O), and C<sub>2</sub>H<sub>6</sub>-CO<sub>2</sub> (2–9 kPa C<sub>2</sub>H<sub>6</sub> and 10 kPa CO<sub>2</sub>) reactions and (b) oxidant pressures in C<sub>2</sub>H<sub>6</sub>-O<sub>2</sub> (1.5–3.5 kPa O<sub>2</sub> and 5 kPa C<sub>2</sub>H<sub>6</sub>), C<sub>2</sub>H<sub>6</sub>-H<sub>2</sub>O (0.8–3.2 kPa H<sub>2</sub>O and 5 kPa C<sub>2</sub>H<sub>6</sub>), and C<sub>2</sub>H<sub>6</sub>-CO<sub>2</sub> (4–16 kPa CO<sub>2</sub> and 5 kPa C<sub>2</sub>H<sub>6</sub>) reactions obtained by Method 1 on 13.5 wt % MoO<sub>x</sub>/Al<sub>2</sub>O<sub>3</sub> catalyst at 873 K (6000 cm<sup>3</sup> h<sup>-1</sup> g<sub>cat</sub><sup>-1</sup>); (c) dependences of  $r(r_{ref})^{-1}$  (eq 11) on C<sub>2</sub>H<sub>6</sub> pressure (2–9 kPa C<sub>2</sub>H<sub>6</sub> and 10 kPa CO<sub>2</sub>) and CO<sub>2</sub> pressure (4–16 kPa CO<sub>2</sub> and 5 kPa C<sub>2</sub>H<sub>6</sub>) in C<sub>2</sub>H<sub>6</sub>-CO<sub>2</sub> reactions obtained by Method 2 on 13.5 wt % MoO<sub>x</sub>/Al<sub>2</sub>O<sub>3</sub> catalyst at 873 K (6000 cm<sup>3</sup> h<sup>-1</sup> g<sub>cat</sub><sup>-1</sup>).

exposure of the MoO<sub>x</sub> catalyst to the reaction mixture, the potential structural transformation of MoO<sub>x</sub>, that is, formation of Mo oxycarbides, Mo carbides, etc., could occur. As the MoO<sub>x</sub> underwent reconstruction, its reactivity for catalyzing each of the various reaction pathways concomitantly changed. After an extended period of time, the selectivities and product distributions became largely unchanged, although all rates, except for those in the C<sub>2</sub>H<sub>6</sub>-O<sub>2</sub> system, continued to decay. This indicates that, at this point, the number of active sites continued to decay, but their reactivity (per site) remained the same. In other words, the deactivation detected in the extended time scale was simply related to the loss of a single type of active site. Thus, the extent of catalyst deactivation in these C<sub>2</sub>H<sub>6</sub> reactions, after initial deactivation, can be represented by a deactivation time constant ( $\alpha_{m,i}$ ; subscript “m” defines the type of reaction, m = total C<sub>2</sub>H<sub>6</sub>, dehydrogenation, combustion, reforming, or hydrogenolysis reaction, and subscript “i” denotes the oxidant chemical identity), with the additional assumption that the deactivation follows a first-order decay,<sup>40,41</sup> where rate is proportional to the surface density of accessible active sites

$$\frac{r_{m,i}}{r_{m,i,0}} = \exp(-\alpha_{m,i}t) \quad (9)$$

where  $r_{m,i}$  is the rate at time-on-stream  $t$ , and  $r_{m,i,0}$  is the rate at zero reaction time ( $t = 0$ ). Figure S2 illustrates the deactivation profiles in C<sub>2</sub>H<sub>6</sub>-CO<sub>2</sub> and C<sub>2</sub>H<sub>6</sub>-H<sub>2</sub>O reactions, fitted with eq 9. The deactivation time constant  $\alpha_{m,i}$  measures the extent of deactivation. The obtained values are presented in Table S1. For total C<sub>2</sub>H<sub>6</sub> turnovers, the deactivation time constants  $\alpha_{total,i}$  (Figure 3a) for the different reaction systems decreased according to the trend of C<sub>2</sub>H<sub>6</sub> > C<sub>2</sub>H<sub>6</sub>-CO<sub>2</sub> > C<sub>2</sub>H<sub>6</sub>-H<sub>2</sub>O and eventually reached near zero for C<sub>2</sub>H<sub>6</sub>-O<sub>2</sub>, as no detectable reactivity loss was observed in oxidehydrogenation catalysis using O<sub>2</sub>. Compared with the system without any oxidant, the introduction of H<sub>2</sub>O or CO<sub>2</sub> mitigates the deactivation but not as effectively as O<sub>2</sub> does. This trend in rate decay mirrors the increase in the oxygen chemical potential at the catalyst surface, a thermodynamic property that dictates the equilibrium surface oxygen contents on the MoO<sub>x</sub> domains. Since the surface

oxygen contents relate directly to the probabilities of these oxygen species to encounter and react with vicinal carbonaceous deposits, the oxygen chemical potential therefore directly regulates the ability of the MoO<sub>x</sub> domains to retard coke formation. Carbon deposition, likely resulting from the formation and dimerization of ethylene, occurs much more prominently in the C<sub>2</sub>H<sub>6</sub>-CO<sub>2</sub> system, gradually decreasing the number of unoccupied sites available for ethane activation. This site decrease, however, does not significantly alter the carbon selectivities, because the identity and reactivity of the active sites remain unchanged during the entire reaction duration, but their density varies with time-on-stream as a consequence of carbon deposition, site occupation, and site loss events.

Since the initial MoO<sub>x</sub> reconstruction and loss of active sites both influence markedly the rates, their analyses, and the resulting mechanistic interpretation, we decouple these effects caused by structural changes, from the intrinsic kinetic dependencies, by probing the rate dependencies of the different catalytic systems using two separate methodologies.

(1) The initial rate method (Method 1), by extrapolating the rate data back to the initial time. The initial rate ( $r_{m,i,0}$ ) reflects the C<sub>2</sub>H<sub>6</sub> turnovers on largely uncovered, pristine sites. Its values are determined by linearizing eq 9, followed by regressing this relation against the rate data in a semilogarithmic plot of rate versus time-on-stream.

(2) The rate ratio method (Method 2), which assesses the rate ratios under two separate conditions—by comparing the rates measured at different reactant pressures ( $r$ ) to a reference rate ( $r_{ref}$ ) value, under conditions in which the reaction occurs on catalyst surfaces with identical structures and coverages of all species, including various carbonaceous debris, and, in turn, instantaneous working site density. This condition is enabled by rapidly switching between the two reaction conditions, as described in detail in Section S4 of the Supporting Information. In this rapid switching mode, it is assumed that any deactivation, caused by the structural transformation of Mo oxide to carbide moieties and by coke deposition and nucleation of larger carbonaceous intermediates, occurs over a much larger time scale than that of the rate measurements (i.e., hours vs minutes). First, this method expresses rate equation ( $r$ ) into two terms, by

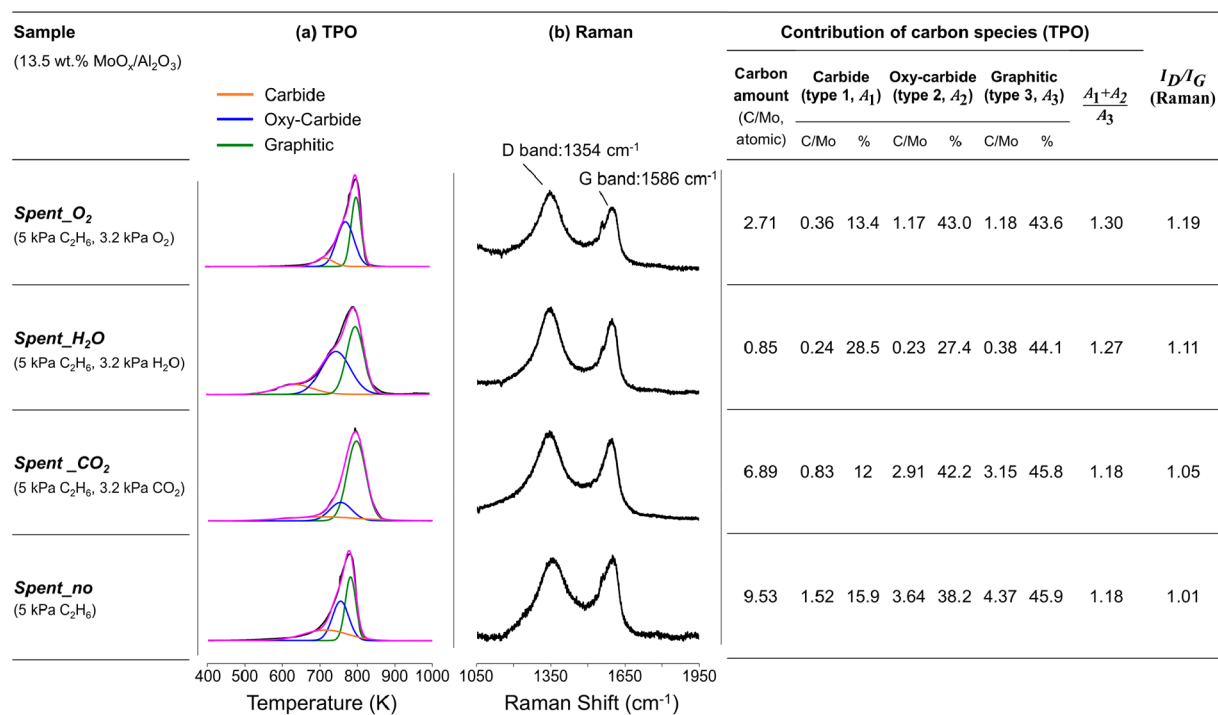


**Figure 5.** (a) TPO profiles and (b) Raman spectra of 13.5 wt % MoO<sub>x</sub>/Al<sub>2</sub>O<sub>3</sub> catalysts after C<sub>2</sub>H<sub>6</sub> (5 kPa) reactions with various oxidants (3.2 kPa O<sub>2</sub>, H<sub>2</sub>O, or CO<sub>2</sub>) and without an oxidant at 873 K for 15 h (6000 cm<sup>3</sup> h<sup>-1</sup> g<sub>cat</sub><sup>-1</sup>).

decoupling its intrinsic component  $r_{\text{int}}$  (per active site) from the rate decay caused by the decrease in active site density. Second, the rate decay  $r_{\text{int}}$  is the product of the intrinsic rate constant  $k_{\text{int}}$  and the partial pressures of ethane and oxidant,  $P_{\text{C}_2\text{H}_6}$  and  $P_{\text{oxidant}}$ , each raised to its respective reaction order  $\alpha$  and  $\beta$ . Third, the decay of active site density is quantitatively described by the instantaneous density of active working sites  $N(t)$ , which depends on the total site density of fresh catalyst  $N_{\text{T}}$  and fraction of poisoned sites,  $\theta_{\text{C}^*}(t)$ . Therefore, the full rate expression is

$$r = r_{\text{int}}N(t) = r_{\text{int}}N_{\text{T}}[1 - \theta_{\text{C}^*}(t)] \\ = k_{\text{int}}P_{\text{C}_2\text{H}_6}^{\alpha}P_{\text{oxidant}}^{\beta}N_{\text{T}}[1 - \theta_{\text{C}^*}(t)] \quad (10a)$$

where

$$N(t) = N_{\text{T}}[1 - \theta_{\text{C}^*}(t)] \quad (10b)$$

Fourth, the rate difference between the two reaction conditions, measured on catalyst surfaces with identical structure and coverages of reactive intermediates, is expressed as their rate ratio  $r(r_{\text{ref}})^{-1}$ . Illustrating this method through the case of C<sub>2</sub>H<sub>6</sub>-CO<sub>2</sub> reactions, the ratio of a rate ( $r$ ), measured at a condition ( $P_{\text{C}_2\text{H}_6}$ ,  $P_{\text{CO}_2}$ ), to that ( $r_{\text{ref}}$ ) at a reference condition ( $P_{\text{C}_2\text{H}_6, \text{ref}}$ ,  $P_{\text{CO}_2, \text{ref}}$ ) at the same temperature is

$$\frac{r}{r_{\text{ref}}} = \frac{r_{\text{int}}}{r_{\text{int,ref}}} = \left(\frac{P_{\text{C}_2\text{H}_6}}{P_{\text{C}_2\text{H}_6, \text{ref}}}\right)^{\alpha} \left(\frac{P_{\text{CO}_2}}{P_{\text{CO}_2, \text{ref}}}\right)^{\beta} \quad (11)$$

The reaction orders for C<sub>2</sub>H<sub>6</sub> and CO<sub>2</sub> ( $\alpha$  and  $\beta$ ) can be determined by simply plotting  $r(r_{\text{ref}})^{-1}$  as a function of C<sub>2</sub>H<sub>6</sub> and CO<sub>2</sub> pressures, respectively, as illustrated in detail in Section S4. We note that this method requires the assumption that, despite a decrease in the working site density, the identity and reactivity of the active site remain the same, irrespective of how their vicinal

sites are being covered with carbon debris. This assumption is valid, as observed from the relatively constant product selectivity values after 4 h time-on-stream (Figure 3c).<sup>42,43</sup>

With the initial rate method (Method 1), Figure 4a,b shows the dependence of C<sub>2</sub>H<sub>4</sub> formation rates on C<sub>2</sub>H<sub>6</sub> and oxidant pressures, respectively, for the different reaction systems. With the rate ratio method (Method 2), Figure 4c shows the  $r(r_{\text{ref}})^{-1}$  ratios (eq 11) for the C<sub>2</sub>H<sub>6</sub>-CO<sub>2</sub> reaction system. The findings from both of these methods, taken together, allow us to probe the intrinsic rate dependencies, by removing corruptions caused by the loss of active sites during catalytic sojourns due to carbon deposition and other reasons. Irrespective of the co-oxidant identity, the intrinsic rates for species  $j$  ( $j = \text{C}_2\text{H}_4, \text{CO}, \text{CO}_2$ , and CH<sub>4</sub>) formation in the C<sub>2</sub>H<sub>6</sub>-O<sub>2</sub> ( $r_{\text{int},j, \text{O}_2}$ ) and C<sub>2</sub>H<sub>6</sub>-CO<sub>2</sub> ( $r_{\text{int},j, \text{CO}_2}$ ) reaction systems all increase proportionally with C<sub>2</sub>H<sub>6</sub> pressure and remain insensitive to the oxidant pressure (Figure 4 and Figures S4-S6 in Section S5 of the Supporting Information). The one exception is for the case of the C<sub>2</sub>H<sub>6</sub>-H<sub>2</sub>O system, where its reaction rates ( $r_{\text{int},j, \text{H}_2\text{O}}$ ) deviate slightly from the linear dependence, as their values increase slightly less than proportionally with the C<sub>2</sub>H<sub>6</sub> pressure (0.9) and display a slight negative dependence on H<sub>2</sub>O pressure (-0.1).

**3.3. Structure of 13.5 wt % MoO<sub>x</sub>/Al<sub>2</sub>O<sub>3</sub> Catalyst after Exposure to C<sub>2</sub>H<sub>6</sub>-O<sub>2</sub>, C<sub>2</sub>H<sub>6</sub>-CO<sub>2</sub>, and C<sub>2</sub>H<sub>6</sub>-H<sub>2</sub>O Reaction Mixtures.** After C<sub>2</sub>H<sub>6</sub>-O<sub>2</sub> (sample *spent\_O2*), C<sub>2</sub>H<sub>6</sub>-CO<sub>2</sub> (sample *spent\_CO2*), and C<sub>2</sub>H<sub>6</sub>-H<sub>2</sub>O (sample *spent\_H2O*) catalysis for 15 h at 873 K, structural changes take place in the MoO<sub>x</sub>/Al<sub>2</sub>O<sub>3</sub> samples, as detected by XRD and high-resolution XPS (Figure 1a,b, respectively). Specifically, two new diffraction peaks appeared at 26.1° and 53.5° in XRD patterns, which can be ascribed to crystalline MoO<sub>2</sub>, suggesting that MoO<sub>x</sub> species were partially reduced during these reactions.<sup>44</sup> These peaks were not present on the spent sample after exposure to C<sub>2</sub>H<sub>6</sub>, without an oxidant (sample *spent\_no*).



oxy-carbide ( $\text{MoO}_x\text{C}_y$ ) phase.<sup>18,44,46</sup> As expected, the sample exposed to only  $\text{C}_2\text{H}_6$  (sample *spent\_no*) contained a large fraction of highly reduced  $\text{Mo}^{\delta+}$  species with oxidation states less than four (28.9%), ascribed to molybdenum oxy-carbides ( $\text{MoC}_x\text{O}_y$ ) or molybdenum carbide ( $\text{Mo}_2\text{C}$ ) species.<sup>47</sup> The presence of carbide or oxy-carbide species can also be confirmed by C 1s spectra (Figure S7) of the same samples, in which a peak at 283.2 eV (Mo–C) was observed.<sup>48</sup> Without an oxidant, the reaction mixture contains predominantly  $\text{C}_2\text{H}_6$ – $\text{C}_2\text{H}_4$ – $\text{H}_2$ ; the chemical composition of this mixture mimics those used for molybdenum oxide carburization, which contain  $\text{H}_2$  and hydrocarbons (e.g.,  $\text{CH}_4$ ,  $\text{C}_2\text{H}_6$ , or  $\text{C}_4\text{H}_{10}$ ) that convert the oxide to carbide.<sup>49–51</sup> Under this highly reducing condition,  $\text{MoO}_x$  species are more likely to be reduced and carburized into amorphous oxy-carbides or carbide phases, undetectable by XRD,<sup>44</sup> and the resulting  $\text{MoO}_x$  moieties in molybdenum oxy-carbide species show low intrinsic reactivity (Figure 4a) in ethane dehydrogenation reaction.<sup>14</sup> As  $\text{MoO}_x$  loses its lattice oxygen atoms, each remaining oxygen binds to the  $\text{MoO}_x$  moieties much more strongly; thus, their reactivity decreases commensurately. This structural transformation most likely caused the drastic change in selectivity observed during the initial period of the reaction (Figure 3c).

Temperature-programmed oxidation gives the  $\text{CO}_2$  evolution profiles and associated carbon contents for the same series of spent catalysts (Figure 5). From the TPO experiments, the carbon content (in C/Mo atomic ratio) of these spent samples decreases for over an order of magnitude from 9.53 to 0.85, starting from the spent sample with the highest amount of carbon in the decreasing order, for samples exposed to  $\text{C}_2\text{H}_6$  (without an oxidant) (*spent\_no*) >  $\text{C}_2\text{H}_6$ – $\text{CO}_2$  (*spent\_CO2*) >  $\text{C}_2\text{H}_6$ – $\text{O}_2$  (*spent\_O2*) >  $\text{C}_2\text{H}_6$ – $\text{H}_2\text{O}$  (*spent\_H2O*), which is in agreement with the XPS-derived surface carbon content, obtained from elemental analysis (Figure 1). Correspondingly, the surface O content, as obtained by XPS surface analysis, shows an inverse trend, once again confirming the lack of significant surface carburization in the presence of oxidant.

Figure 5b shows the Raman spectra of these spent catalysts. Two major bands, which correspond to the D and G bands of carbon, are observed. The shift at  $\sim 1586\text{ cm}^{-1}$  (G band) is related to the vibration of  $\text{sp}^2$ -bonded carbon atoms in a two-dimensional hexagonal lattice, indicative of the presence of a crystalline graphite phase.<sup>52</sup> The D band, located at  $\sim 1354\text{ cm}^{-1}$ , is commonly assigned to structurally disordered (amorphous) carbon.<sup>52</sup> The presence of these two bands indicates the heterogeneity of the carbon species formed on  $\text{MoO}_x$  during ethane reactions. The intensity ratios (height ratios) of D to G band, that is,  $I_D/I_G$  values, as shown in Figure 5, are in the range of 1.01–1.19 on all spent samples, suggesting that similar types of coke deposited after various  $\text{C}_2\text{H}_6$  reaction systems. The TPO profiles in Figure 5a show three types of deposited carbon species—the  $\text{CO}_2$  evolution at the lower temperature of  $\sim 680\text{ K}$  can be typically attributed to the molybdenum carbide species (type 1),<sup>53</sup> while that at  $\sim 750\text{ K}$  can be attributed to nonrefractory (soft) coke or oxy-carbide species (type 2).<sup>44</sup> The peak at higher temperature ( $\sim 780\text{ K}$ ) can be ascribed to the presence of graphitic coke,<sup>54</sup> as suggested by the presence of the G band on the Raman spectra.  $A_1$ ,  $A_2$ , and  $A_3$  denote the C/Mo atomic ratio for these three types of carbon, respectively. The atomic ratio of carbon species evolved at lower temperatures (types 1 and 2) to that at the higher temperature (type 3),  $(A_1 + A_2)/A_3$ , reflects the ratio of amorphous to crystalline carbon; these ratios for different reaction systems are

listed in Figure 5. The values obtained (1.18–1.30) are in good agreement with those observed during Raman analysis on the same samples ( $I_D/I_G = 1.01$ – $1.19$ ).

**3.4. A Generalized Mechanistic Framework for  $\text{C}_2\text{H}_6$ ,  $\text{C}_2\text{H}_6$ – $\text{O}_2$ ,  $\text{C}_2\text{H}_6$ – $\text{CO}_2$ , and  $\text{C}_2\text{H}_6$ – $\text{H}_2\text{O}$  Catalysis—Three Tandem Catalytic Cycles.** We propose, in Scheme 1, a generalized mechanistic framework that captures the catalytic sojourns of ethane dehydrogenation and oxidehydrogenation on dispersed molybdenum oxide surfaces, which contains three tandem, kinetically coupled cycles of ethane activation (cycle 1), oxidant activation (cycle 2), and carbon removal (cycle 3). As revealed by Raman and UV–vis analyses, isolated and oligomeric  $\text{MoO}_x$  species coexist on  $\text{Al}_2\text{O}_3$  surfaces. Although it is generally accepted that  $\text{C}_2\text{H}_6$  activates on a lattice oxygen, and the catalytic reactivity depends largely on the binding energy of this oxygen atom,<sup>8,11</sup> we are unable to pinpoint the exact location of the active lattice oxygen and its associated Mo structure, for example, isolated, oligomeric, or bulk  $\text{MoO}_x$  domains, that are most effective for  $\text{C}_2\text{H}_6$  activation. For simplification, an isolated  $\text{MoO}_x$  is used to represent the active site when describing the mechanisms in Scheme 1. On the basis of the similar rate dependencies (Figure 4 and Figures S4–S6) for the formation of each product across the three  $\text{C}_2\text{H}_6$  reaction systems (with  $\text{O}_2$ ,  $\text{H}_2\text{O}$ , or  $\text{CO}_2$ ) and, for each reaction system, constant selectivities attained above 4 h time-on-stream, we hypothesize that C–H bond activation in  $\text{C}_2\text{H}_6$  remains as the kinetically relevant step for ethane dehydrogenation, oxidehydrogenation, and for the much slower reforming or hydrogenolysis reactions in all three catalytic systems. The difference in  $\text{C}_2\text{H}_6$  conversion rates across these catalytic systems must arise from the different extents of the undesired  $\text{C}_2\text{H}_x^*$  oligomerization, which produces unwanted carbonaceous debris, or from site occupation by other intermediates. The carbon content deposited on catalyst surfaces depends directly on the oxygen chemical potential, a thermodynamic property that rigorously dictates the actual concentration of the oxygen species at the catalyst surfaces and their reactivity in oxidizing and removing the carbon debris.

**Cycle 1: Ethane Activation.** In the *Ethane Activation* cycle (cycle 1), ethane first adsorbs by interacting with a lattice oxygen site ( $\text{O}_{\text{lattice}}^*$ ) of dispersed  $\text{MoO}_x$  moieties in a quasi-equilibrated step (Step E1). Next, a neighboring lattice oxygen assists with the kinetically relevant C–H bond cleavage of ethane, by abstracting one of its hydrogens (Step E2). The first-order rate dependence suggests that  $\text{C}_2\text{H}_6$  activation on  $\text{MoO}_x$  surfaces saturated with lattice oxygen atoms limits rates, as previously reported for  $\text{C}_2\text{H}_6$ – $\text{O}_2$  and  $\text{C}_3\text{H}_8$ – $\text{O}_2$  reactions catalyzed by  $\text{MoO}_x$ ,<sup>55</sup>  $\text{VO}_x$ ,<sup>55–58</sup>  $\text{WO}_x$ ,<sup>55</sup> and  $\text{MoVTeNbO}_x$ <sup>58</sup> catalysts. The lack of  $\text{C}_3\text{H}_{8-x}\text{D}_x$  ( $0 < x < 8$ ) mixed isotopomer formation during  $\text{C}_3\text{H}_8$ – $\text{C}_3\text{D}_8$ – $\text{O}_2$  reactions on  $\text{MoO}_x/\text{ZrO}_2$ <sup>59</sup> confirms that the initial C–H bond activation (Step E2) is not only a kinetically relevant but also an irreversible step in this cycle, consistent with the highest barrier found for this initial C–H dissociation of alkanes (ethane and propane) than any other elementary steps involved in ODH catalyzed by  $\text{MoO}_x$  clusters,<sup>60</sup>  $\text{V}_2\text{O}_5(001)$  surface,<sup>61,62</sup>  $\text{V}_2\text{O}_5(010)$  surface,<sup>63</sup> and  $\text{V}_2\text{O}_5$  dimers.<sup>64</sup> After the initial C–H bond cleavage, a  $\beta$ -hydride elimination step (Step E3) evolves the ethylene, leaving a total of two hydroxyl species at the Mo center. These hydroxyl species recombine and desorb as  $\text{H}_2$  (Step E4), leaving behind two oxygen sites. This cycle, when coupled with the *Carbon Removal* cycle, describes the ethane dehydrogenation reaction (eq 1). When coupled with both the *Oxidant Activation* and *Carbon*

Removal cycles (cycles 2 and 3, respectively), it describes the  $C_2H_6-O_2$  (eq 2),  $C_2H_6-CO_2$  (eq 4a), and  $C_2H_6-H_2O$  (eq 4b) systems.

Figure 6a,b shows the reactant and product evolution and the rates of oxygen vacancy ( $\square$ ) formation from  $MoO_x$ ,

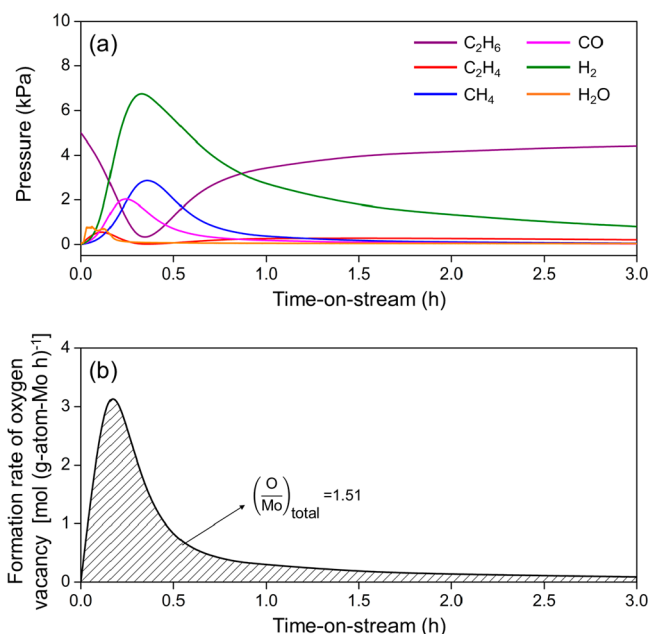


**Figure 6.** (a)  $C_2H_6$  reactant and product concentrations and (b) rates of oxygen vacancy formation, which equal the rates of lattice oxygen removal from the  $MoO_x$  to evolve oxygen-containing products ( $H_2O$  and  $CO$ ), plotted as a function of time-on-stream during transient  $C_2H_6$  (without an oxidant) reactions at 873 K (5 kPa  $C_2H_6$ , 13.5 wt %  $MoO_x/Al_2O_3$  catalyst,  $6000\text{ cm}^3\text{ h}^{-1}\text{ g}_{cat}^{-1}$ ).

respectively, during transient  $C_2H_6$  dehydrogenation reaction (without an oxidant) on the 13.5 wt %  $MoO_x/Al_2O_3$  catalyst at 873 K. Upon the initial  $C_2H_6$  introduction,  $C_2H_4$ ,  $CH_4$ , and  $H_2$  were detected together with the oxygen-containing products  $CO$  and  $H_2O$ . These oxygen-containing products were formed because of lattice oxygen involvement in ethane activation catalysis; thus,  $CO$  and  $H_2O$  formation rates equal the lattice oxygen removal rates, presented in Figure 6b as the oxygen vacancy ( $\square$ ) formation rates. During the first 30 min of  $C_2H_6$  exposure, a large amount of  $H_2$  formed; however, during this time interval  $C_2H_4$  was not detected in the reactor effluent, indicating significant carbon deposition onto the catalyst. During this interval,  $C_2H_6$  reacted with a portion of  $MoO_x$  converting it to molybdenum carbide in a noncatalytic process, as established previously.<sup>49–51</sup> After the first 0.5 h, when a portion of molybdenum oxide ( $\sim 32\%$  Mo) was converted to carbide or oxy-carbide,  $C_2H_4$  began to appear, and, as a result, the  $H_2$ -to- $C_2H_4$  ratio began to decrease (e.g., to 2.2 at 15 h), approaching but not reaching unity, the value expected for dehydrogenation stoichiometry, because of continuous carbon deposition in the absence of oxidant. The total number of oxygen vacancies on  $MoO_x$ , which equals the cumulative amount of oxygen vacancy formed over the entire initial reaction period (0–3 h), is 1.51  $\square/Mo$  atomic ratio, determined from integrating the oxygen vacancy formation rate evolution profile, as shown in Figure 6b. This value is consistent with a  $\square/Mo$  ratio of 1.50 obtained from a separate oxygen vacancy titration study (described in Section S7 of the Supporting Information),

performed after reducing the catalyst in  $H_2$  at the same temperature for 2 h. These  $\square/Mo$  ratios, given by both the transient  $C_2H_6$  dehydrogenation reaction and oxygen vacancy titration study, give an average Mo oxidation state of ca. +3, which is close to that of +3.89 determined from XPS analysis on  $MoO_x$  catalyst, after 15 h  $C_2H_6$  reaction (no oxidant) at 873 K (spent no, Figure 1), where a large portion of Mo (28.9%) was below +4, which can be assigned to Mo oxidation states in molybdenum oxy-carbide ( $Mo^{3+}$ ) or carbide ( $Mo^{2+}$ ) species.<sup>18</sup>

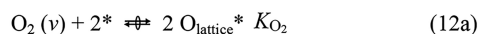
**Cycle 2: Oxidant Activation.** The difference among  $C_2H_6-O_2$ ,  $C_2H_6-CO_2$ , and  $C_2H_6-H_2O$  catalysis lies in the mechanism to which the reduced Mo undergoes reoxidation via Oxidant Activation cycle (cycle 2), during which the oxidant  $O_2$ ,  $CO_2$ , or  $H_2O$  activates and removes carbonaceous debris from the catalyst surfaces.

$O_2$ , when used as an oxidant in the ethane ODH reaction (cycle 2- $O_2$ ), dissociates via an irreversible  $O_2$  dissociation step (Step O1), as confirmed from negligible  $^{16}O_2$ - $^{18}O_2$  scrambling during  $C_3H_8$ - $^{16}O_2$ - $^{18}O_2$  isotopic exchange probe reactions on an  $MoO_x/ZrO_2$  catalyst.<sup>59</sup> Moreover, the barrier for oxygen dissociation on the oxygen vacancy sites of  $MoO_3$  (010) surface is 0.90 eV with a large negative free energy change ( $\Delta G = -3.63$  eV, 623 K),<sup>65</sup> suggesting that this step is irreversible.

$CO_2$ , when used as an oxidant (cycle 2- $CO_2$ ), activates on either a lattice oxygen (pathway  $CO_2$ -a) or a hydroxy group (pathway  $CO_2$ -b). In the  $CO_2$ -a pathway,  $CO_2$  adsorbs on a lattice oxygen,  $O_{lattice}$ , as a carbonate ( $CO_3^*$ ) intermediate (Step O4a), followed by  $OC=O^1$  bond cleavage and then the transfer of the  $O^1$  to a neighboring reduced Mo center, leaving an adsorbed  $CO^*$  on the  $O_{lattice}$  site ( $OCO^*$ , Step O5a), which subsequently desorbs as  $CO$  to regenerate the  $O_{lattice}$  (Step O6). In the alternate  $CO_2$ -b pathway, a hydroxyl hydrogen assists with  $CO_2$  activation, forming a  $COOH$  intermediate adsorbed at an oxygen site ( $HCO_3^*$ , Step O4b), followed by its decomposition to  $OH^*$  and  $OCO^*$  (Step O5b) before the desorption of  $CO^*$  and regeneration of the  $O_{lattice}$  (Step O6).

$H_2O$ , when used as a coreactant (cycle 2- $H_2O$ ), dissociates on an oxygen vacancy and a lattice oxygen site pair to produce two  $OH^*$  groups (Step O2) that then recombine to desorb as  $H_2$  (Step O3). In contrast to using  $O_2$  or  $CO_2$  oxidant,  $H_2O$  dissociation does not generate reactive oxygen species required for carbon oxidation and removal in cycle 3. The dissociation also does not replenish and retain  $O_{lattice}$  on  $MoO_x$  and instead, it converts them into hydroxyl species.

Embedded within these  $CO_2$  and  $H_2O$  activation cycles (cycles 2- $CO_2$  and 2- $H_2O$ ) are the elementary steps for the water-gas shift reaction in both the forward and reverse directions (Steps O2-O3, O4a-O5a or O4b-O5b, and O6), and their rates directly reflect the oxygen contents on  $MoO_x$ . The oxygen chemical potential is quantitatively represented by the oxygen virtual pressure ( $P_{O_2(v)}$ , eqs 12a and 12b), a fictitious



oxygen pressure that is in equilibrium with the instantaneous  $O_{lattice}^*$ -to- $^*$  ratio during steady-state  $C_2H_6-CO_2$  and  $C_2H_6-H_2O$  catalysis,  $[O^*]/[^*]_{steady-state\ catalysis}$

$$\frac{[O^*]}{[^*]_{steady-state\ catalysis}} = \left( K_{O_2} \frac{P_{O_2(v)}}{P^\theta} \right)^{0.5} \quad (12b)$$

where  $P^\theta$  is the standard atmosphere. When the WGS reaction reaches chemical equilibrium, the oxygen content,  $[O^*]/$

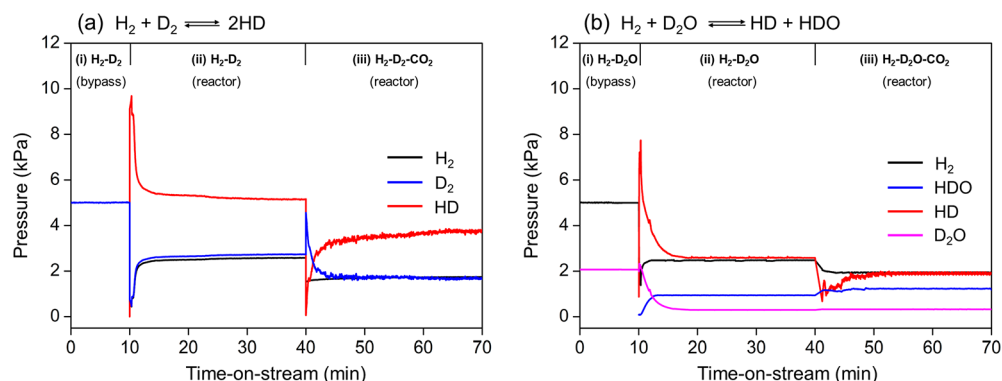


**Figure 7.** (a) The partial pressures of dihydrogen isotopomers of (i)  $\text{H}_2\text{-D}_2$  (5 kPa  $\text{H}_2$ , 5 kPa  $\text{D}_2$ ) feed mixture bypassing the reactor, (ii) during  $\text{H}_2\text{-D}_2$  (5 kPa  $\text{H}_2$ , 5 kPa  $\text{D}_2$ ) reactions, and (iii) during  $\text{H}_2\text{-D}_2\text{-CO}_2$  (5 kPa  $\text{H}_2$ , 5 kPa  $\text{D}_2$ , 10 kPa  $\text{CO}_2$ ) reactions. (b) The partial pressures of dihydrogen and water isotopomers of (i)  $\text{H}_2\text{-D}_2\text{O}$  (5 kPa  $\text{H}_2$ , 2 kPa  $\text{D}_2\text{O}$ ) feed mixture bypassing the reactor, (ii) during  $\text{H}_2\text{-D}_2\text{O}$  (5 kPa  $\text{H}_2$ , 2 kPa  $\text{D}_2\text{O}$ ) reactions, and (iii) during  $\text{H}_2\text{-D}_2\text{O-CO}_2$  (5 kPa  $\text{H}_2$ , 2 kPa  $\text{D}_2\text{O}$ , 10 kPa  $\text{CO}_2$ ) reactions (13.5 wt %  $\text{MoO}_x/\text{Al}_2\text{O}_3$  catalyst, 873 K,  $6000 \text{ cm}^3 \text{ h}^{-1} \text{ g}_{\text{cat}}^{-1}$ ).

$[\text{O}^*]_{\text{steady-state catalysis, WGS, eq}}$  where subscript *WGS, eq* denotes equilibrium, equals

$$\begin{aligned} \frac{[\text{O}^*]}{[\text{O}^*]_{\text{steady-state catalysis, WGS, eq}}} &= K_{\text{CO}_2\text{-CO}} \left( \frac{P_{\text{CO}_2}}{P_{\text{CO}}} \right)_{\text{WGS, eq}} \\ &= K_{\text{H}_2\text{O-H}_2} \left( \frac{P_{\text{H}_2\text{O}}}{P_{\text{H}_2}} \right)_{\text{WGS, eq}} \end{aligned} \quad (13)$$

where  $K_{\text{CO}_2\text{-CO}}$  and  $K_{\text{H}_2\text{O-H}_2}$  are the equilibrium constants for  $2\text{CO}_2 \leftrightarrow 2\text{CO} + \text{O}_2$  (Step C1 + Step O1 in Scheme 1) and  $2\text{H}_2\text{O} \leftrightarrow 2\text{H}_2 + \text{O}_2$  (Step O1 + Step O2 + Step O3 in Scheme 1) reactions, respectively. At WGS equilibrium, the  $\text{O}_2$  virtual pressure is on the order of  $10^{-22}$  kPa, (e.g.,  $1.45 \times 10^{-22}$  kPa, estimated by assuming WGS reaction reaches its equilibrium during  $\text{C}_2\text{H}_6\text{-CO}_2$  catalysis, with 3.2 kPa  $\text{CO}_2$  and 1.7 kPa  $\text{H}_2$  (the product of ethane dehydrogenation) as the feed composition at 873 K. Since the WGS reaction does not reach chemical equilibrium, as evidenced from the approach-to-equilibrium values that are much lower than unity, during  $\text{C}_2\text{H}_6\text{-CO}_2$  catalysis ( $\eta_{\text{RWGS}}$ , eq 8a, 0.08–0.18) and during  $\text{C}_2\text{H}_6\text{-H}_2\text{O}$  catalysis ( $\eta_{\text{WGS}}$ , eq 8b, 0.04–0.08) at 873 K, at least one of the elementary steps within the WGS catalytic cycle (in the forward and reverse directions) does not reach equilibrium. Thus, oxygen chemical potentials at the catalyst surfaces,  $P_{\text{O}_2(\text{v})}$ , and  $[\text{O}^*]/[\text{O}^*]_{\text{steady-state catalysis}}$  are much lower than those dictated by the water–gas shift equilibrium.

$$\begin{aligned} \left[ \frac{[\text{O}^*]}{[\text{O}^*]_{\text{steady-state catalysis}}} \right] &= \left( K_{\text{O}_2} \frac{P_{\text{O}_2}}{P^\theta} \right)^{0.5} \\ &< \left[ K_{\text{CO}_2\text{-CO}} \left( \frac{P_{\text{CO}_2}}{P_{\text{CO}}} \right)_{\text{WGS, eq}} \right] = K_{\text{H}_2\text{O-H}_2} \left( \frac{P_{\text{H}_2\text{O}}}{P_{\text{H}_2}} \right)_{\text{WGS, eq}} \\ &= \left[ \frac{[\text{O}^*]}{[\text{O}^*]_{\text{steady-state catalysis, WGS, eq}}} \right] \end{aligned} \quad (14)$$

Isotopic exchange reactions with  $\text{H}_2\text{-D}_2$ ,  $\text{H}_2\text{-D}_2\text{-CO}_2$ ,  $\text{H}_2\text{-D}_2\text{O}$ , and  $\text{H}_2\text{-D}_2\text{O-CO}_2$  mixtures probe the reversibility of the

$\text{H}_2\text{O}$  and  $\text{H}_2$  activation within the oxidant activation cycles. During  $\text{H}_2\text{-D}_2$  reactions (5 kPa each, 873 K), dihydrogen isotopomer distributions attain binominal distributions (2.58  $\text{H}_2$ /4.85  $\text{HD}$ /2.58  $\text{D}_2$ ) identical to those expected at equilibrium of 2.52  $\text{H}_2$ /4.96  $\text{HD}$ /2.52  $\text{D}_2$ , within the experimentally measurable accuracy, as shown in Figure 7a. These distributions correspond to an approach-to-equilibrium for  $\text{H}_2\text{-D}_2$  exchange of 0.92. Incorporating  $\text{CO}_2$  (10 kPa) into the  $\text{H}_2\text{-D}_2$  feed mixture leads to dihydrogen isotopomer distributions of 1.84  $\text{H}_2$ /3.52  $\text{HD}$ /1.70  $\text{D}_2$  and an approach-to-equilibrium of 1.16. Thus, the hydrogen dissociation-recombination step is quasi-equilibrated (Steps E4 and O3). Similarly, the  $\text{H}_2\text{-D}_2\text{O}$  (5 kPa  $\text{H}_2$ , 2 kPa  $\text{D}_2\text{O}$ ) and  $\text{H}_2\text{-D}_2\text{O-CO}_2$  (5 kPa  $\text{H}_2$ , 2 kPa  $\text{D}_2\text{O}$ , 10 kPa  $\text{CO}_2$ ) reactions, which probe the reversibility of  $\text{H}_2\text{O}$  activation, lead to the effluent  $\text{H}_2/\text{D}_2\text{O}/\text{HD}/\text{HDO}$  isotopomer distributions of 2.48:0.30:2.59:0.95 and 1.95:0.33:1.94:1.10, which translate to approach-to-equilibrium values of 1.09 and 1.10, respectively. These isotopic exchange results suggest that the  $\text{H}_2\text{O}$  activation step (Step O2) is quasi-equilibrated (Figure 7b).

The reversible steps for water formation are in agreement with the observed water inhibition effects during  $\text{C}_2\text{H}_6\text{-H}_2\text{O}$  catalysis (Figure 4b) and with those observed when introducing water into the feed during  $\text{C}_2\text{H}_6\text{-O}_2$  catalysis on  $\text{VO}_x/\text{Al}_2\text{O}_3$ <sup>66</sup> and during  $\text{C}_3\text{H}_8\text{-O}_2$  catalysis on  $\text{MoO}_x/\text{ZrO}_2$ <sup>55</sup> and  $\text{VO}_x/\text{ZrO}_2$ .<sup>57</sup> On the Mo (010) surface, density functional theory (DFT) studies show that two surface hydroxy groups recombine to form a water (Step O2) with an extremely low barrier of 0.10 eV and a free energy change of  $-0.02$  eV (623 K).<sup>65</sup> Thus,  $\text{H}_2\text{O}$  converts the reactive oxygen species to inactive surface hydroxyls, inhibiting the  $\text{C}_2\text{H}_6$  turnovers; it also does not assist with the removal of carbonaceous debris, as its activation does not generate reactive oxygen species. These findings are consistent with both the low reactivity and low carbon deposition after  $\text{C}_2\text{H}_6\text{-H}_2\text{O}$  catalysis.

The quasi-equilibrated nature of hydrogen and water activation further confirms that, within the RWGS catalytic cycle embedded in this *Oxidant Activation* cycle,  $\text{CO}_2$  activation (Step O5a or O5b, forward) limits rate. Similarly, the WGS catalysis during  $\text{C}_2\text{H}_6\text{-H}_2\text{O}$  reactions must also be limited by  $\text{CO}_2$  formation (Step O5a or O5b, reverse). This finding is in contrast to those expected on late transition metals, Pt,<sup>67</sup> Ni,<sup>68</sup> Co,<sup>68,69</sup> and Ru,<sup>70</sup> as those metals catalyze the water–gas shift reaction effectively under comparable conditions (773–873 K), often attaining chemical equilibriums at all conditions relevant to alkane-reforming catalysis.

**Table 1.** Deactivation Constants ( $\alpha_{\text{deh},i}$ , eq 9), Intrinsic Rate Expressions (eqs S9–S11), Rate and Equilibrium Parameters, C–H Bond Activation Barriers, and Expressions of \*-to-O\* and OH\*-to-O\* Coverage Ratios for the Rate Expressions (eq 15) during C<sub>2</sub>H<sub>6</sub>–O<sub>2</sub>, C<sub>2</sub>H<sub>6</sub>–CO<sub>2</sub>, and C<sub>2</sub>H<sub>6</sub>–H<sub>2</sub>O Reactions on 13.5 wt % MoO<sub>x</sub>/Al<sub>2</sub>O<sub>3</sub> Catalyst

	Deactivation constant ( $\alpha_{\text{deh},i}$ ) <sup>a</sup>	Intrinsic rate expression ( $r_{\text{int},\text{C}_2\text{H}_6,i}$ ) <sup>a</sup>	$k_{\text{E}2}K_{\text{E}1}$ [mmol (g-atom-Mo s kPa) <sup>-1</sup> ] <sup>a</sup>	$K_{\text{O}3}^{-1a}$	Activation barrier [kJ mol <sup>-1</sup> ]	$\frac{[*]}{[\text{O}^*]}$	$\frac{[\text{OH}^*]}{[\text{O}^*]}$
C <sub>2</sub> H <sub>6</sub> –O <sub>2</sub>	0	$k_{\text{E}2}K_{\text{E}1}P_{\text{C}_2\text{H}_6}$	0.265	-	101	$\left(\frac{k_{\text{E}2}K_{\text{E}1}P_{\text{C}_2\text{H}_6}}{2k_{\text{O}1}P_{\text{O}_2}}\right)^{0.5}$	$\left(\frac{P_{\text{H}_2}}{K_{\text{E}4}}\right)^{0.5}$
C <sub>2</sub> H <sub>6</sub> –CO <sub>2</sub>	0.09	$k_{\text{E}2}K_{\text{E}1}P_{\text{C}_2\text{H}_6}$	0.119	-	105	$\frac{K_{\text{E}1}k_{\text{E}2}K_{\text{O}6}P_{\text{C}_2\text{H}_6} + k_{\text{O}5a,r}P_{\text{CO}}}{k_{\text{O}5a,r}K_{\text{O}4a}K_{\text{O}6}P_{\text{CO}_2}}$ (pathway a)	$\left(\frac{P_{\text{H}_2}}{K_{\text{E}4}}\right)^{0.5}$
						$\frac{k_{\text{O}5b,r}K_{\text{O}6}P_{\text{CO}}P_{\text{H}_2}^{0.5} - 2k_{\text{E}2}K_{\text{E}1}K_{\text{O}6}P_{\text{C}_2\text{H}_6}K_{\text{E}4}^{0.5}}{k_{\text{O}5b,r}K_{\text{O}4b}P_{\text{CO}_2}P_{\text{H}_2}^{0.5}}$ (pathway b)	$\left(\frac{P_{\text{H}_2}}{K_{\text{E}4}}\right)^{0.5}$
C <sub>2</sub> H <sub>6</sub> –H <sub>2</sub> O	0.09	$\frac{k_{\text{E}2}K_{\text{E}1}P_{\text{C}_2\text{H}_6}}{[1 + (K_{\text{O}3}^{-1}P_{\text{H}_2})^{0.5}]}$	0.122	0.0189	123	$\frac{P_{\text{H}_2}}{K_{\text{O}2}K_{\text{O}3}P_{\text{H}_2\text{O}}}$	$\left(\frac{P_{\text{H}_2}}{K_{\text{O}3}}\right)^{0.5}$

<sup>a</sup>873 K.

**Cycle 3: Carbon Removal.** The reactive oxygen species formed in the *Oxidant Activation* cycle are being consumed in the *Carbon Removal* cycle. In this cycle, oxygen species migrate to and react with adjacent carbon atoms (C\*), forming CO\* species before CO desorption (Steps C2 and C3). The steps for CO<sub>2</sub> activation to CO (Step C1), together, describe the reverse Boudouard reaction (CO<sub>2</sub> + C → 2CO). Carbon deposition is more severe in C<sub>2</sub>H<sub>6</sub>–CO<sub>2</sub> than in C<sub>2</sub>H<sub>6</sub>–O<sub>2</sub> reactions (C/Mo atomic ratio of 6.89 vs 2.71, respectively), because of the much less effective CO<sub>2</sub> activation (compared to O<sub>2</sub>), given by the lower O<sub>2</sub> virtual pressure (on the order of 10<sup>-22</sup> kPa vs 1.75–1.80 kPa O<sub>2</sub> during C<sub>2</sub>H<sub>6</sub>–O<sub>2</sub> reactions) for generating reactive oxygen species.

**3.5. Generalized Rate Expression for Ethane Oxidative Dehydrogenation with Various Oxidants (O<sub>2</sub>, CO<sub>2</sub>, H<sub>2</sub>O) on 13.5 wt % MoO<sub>x</sub>/Al<sub>2</sub>O<sub>3</sub> Catalyst.** All reaction systems share an identical kinetically relevant C–H activation step (Step E2) assisted by a lattice oxygen atom, but their relative surface abundances of [\*], [OH\*], and [C\*] differ. The mechanistic similarities in Scheme 1 lead to a time-dependent generalized rate expression for ethylene site-time-yield ( $r_{\text{C}_2\text{H}_6,i}$ ,  $i = \text{O}_2, \text{CO}_2, \text{or H}_2\text{O}$ ) during C<sub>2</sub>H<sub>6</sub>–O<sub>2</sub>, C<sub>2</sub>H<sub>6</sub>–CO<sub>2</sub>, or C<sub>2</sub>H<sub>6</sub>–H<sub>2</sub>O catalysis (eq 15), accounting for the loss of active site during steady-state catalysis (as a function of time-on-stream  $t$ ) of

$$r_{\text{C}_2\text{H}_6,i} = r_{\text{int},\text{C}_2\text{H}_6,i} \times N(t) = r_{\text{int},\text{C}_2\text{H}_6,i} \times N_{\text{T}} \exp(-\alpha_{\text{deh},i}t) \\ = \frac{k_{\text{E}2}K_{\text{E}1}P_{\text{C}_2\text{H}_6}[\text{O}^*]^2}{([\text{O}^*] + [*] + [\text{OH}^*])^2} \times N_{\text{T}} \exp(-\alpha_{\text{deh},i}t) \quad (15)$$

This rate expression contains two parts, that is, an intrinsic rate term ( $r_{\text{int},\text{C}_2\text{H}_6,i}$ ), which captures catalysis on uncovered MoO<sub>x</sub> and a time-dependent term [ $N_{\text{T}} \exp(-\alpha_{\text{deh},i}t)$ ], which accounts for the time-dependent working site density  $N(t)$ , as derived in Section S8 of the Supporting Information.  $k_{\text{E}2}$  is the rate constant of Step E2, and  $K_{\text{E}1}$  is the equilibrium constant of Step

E1, as defined in Scheme 1;  $N_{\text{T}}$  is the number of total active sites in the fresh MoO<sub>x</sub> catalyst. The time-dependent term captures the reduction of working, catalytically active sites due to carbon deposition. The individual expressions for the [OH\*]-to-[O\*] and [\*]-to-[O\*] coverage ratios differ among these reaction systems with their exact formulas summarized in Table 1.

For the C<sub>2</sub>H<sub>6</sub>–O<sub>2</sub> and C<sub>2</sub>H<sub>6</sub>–CO<sub>2</sub> reaction systems, the intrinsic rate expressions  $r_{\text{int},\text{C}_2\text{H}_6,\text{O}_2}$  and  $r_{\text{int},\text{C}_2\text{H}_6,\text{CO}_2}$  both reduce to first-order dependence on C<sub>2</sub>H<sub>6</sub> pressure and zeroth-order dependence on coreactant pressure (eqs S9 and S10), because O\* is the most abundant surface intermediate (MASI). These expressions are mechanistically analogous to those reported during ethane ODH on VO<sub>x</sub><sup>56,58</sup> and MoVTenbO<sup>58</sup> and propane ODH on MoO<sub>x</sub>, VO<sub>x</sub>, and WO<sub>x</sub> catalysts.<sup>55,57,59</sup> On such surfaces, increasing the oxidant pressure alters neither the lattice oxygen concentrations nor the resulting turnover rates (when normalized to the catalytically available sites). Nonlinear regression analyses of the rate data (Figures 3a and 4a,b) during C<sub>2</sub>H<sub>6</sub>–O<sub>2</sub> and C<sub>2</sub>H<sub>6</sub>–CO<sub>2</sub> catalysis give the fitted rate profiles in Figure 3a, the time-dependent behavior in Figure 9, kinetic parameters in Table 1, and the parity plots in Figure S8. The value of  $K_{\text{E}1}k_{\text{E}2}$  in C<sub>2</sub>H<sub>6</sub>–O<sub>2</sub> catalysis is higher than that in C<sub>2</sub>H<sub>6</sub>–CO<sub>2</sub> catalysis at 873 K, most likely caused by the presence of additional fraction of active sites (lattice oxygen), available only in the presence of O<sub>2</sub> but not in the presence of CO<sub>2</sub> oxidant.

During C<sub>2</sub>H<sub>6</sub>–H<sub>2</sub>O catalysis, a portion of the O\* is converted to hydroxy (OH\*), and both of these species coexist at substantial surface coverages as the MASI. As a result, the intrinsic rate expression  $r_{\text{int},\text{C}_2\text{H}_6,\text{H}_2\text{O}}$  deviates from the first-order dependence.

$$r_{\text{int,C}_2\text{H}_4,\text{H}_2\text{O}} = \frac{k_{\text{E2}}K_{\text{E1}}P_{\text{C}_2\text{H}_6}[\text{O}^*]^2}{([\text{O}^*]+[\text{O}^*]+[\text{OH}^*])^2} = \frac{k_{\text{E2}}K_{\text{E1}}P_{\text{C}_2\text{H}_6} \left( \frac{K_{\text{O}_2}K_{\text{O}_3}P_{\text{H}_2\text{O}}}{P_{\text{H}_2}} \right)^2}{\left( \frac{K_{\text{O}_2}K_{\text{O}_3}P_{\text{H}_2\text{O}}}{P_{\text{H}_2}} + \frac{K_{\text{O}_2}K_{\text{O}_3}^{0.5}P_{\text{H}_2\text{O}}}{P_{\text{H}_2}^{0.5}} \right)^2} = \frac{k_{\text{E2}}K_{\text{E1}}P_{\text{C}_2\text{H}_6}}{[1+(K_{\text{O}_3}^{-1}P_{\text{H}_2})^{0.5}]^2} \quad (16)$$

Nonlinear regression of this intrinsic rate expression and its time-dependent full rate expression (eq 15) against the rate data (Figures 3a and 4a,b) during  $\text{C}_2\text{H}_6\text{-H}_2\text{O}$  reactions gives the predicted rate profile in Figure 3a, the time-dependent behavior in Figure 9, and the  $K_{\text{O}_3}^{-1}$  value of 0.0188 at 873 K. This value, together with the operating  $\text{C}_2\text{H}_6$  and  $\text{H}_2$  pressures (3–9 kPa of  $\text{C}_2\text{H}_6$  and 0.4–0.9 kPa of  $\text{H}_2$ ), gives  $\text{OH}^*$  fractional coverages ranging from 0.11 to 0.18, consistent with the observed water inhibitive effect (Figure 4b). The similar values of  $K_{\text{E1}}k_{\text{E2}}$  in  $\text{C}_2\text{H}_6\text{-CO}_2$  and  $\text{C}_2\text{H}_6\text{-H}_2\text{O}$  reactions at 873 K indicate that these reactions share the same kinetically relevant step of C–H bond activation and that the identity of the oxidants does not affect the intrinsic rate, but instead it affects the removal of the carbonaceous intermediates, surface densities of actual working sites, and in turn the time-dependent term  $[N_{\text{T}} \exp(-\alpha_{\text{deh},i} t)]$  in the full rate expression (eq 15).

The first-order, intrinsic rate coefficient for ethylene formation ( $k_{\text{int,C}_2\text{H}_4,i}^{\text{1st}}$ ) is defined by the intrinsic ethylene formation rate ( $r_{\text{int,C}_2\text{H}_4,i}$ , per total Mo atom) divided by the  $\text{C}_2\text{H}_6$  pressure ( $P_{\text{C}_2\text{H}_6}$ ):

$$k_{\text{int,C}_2\text{H}_4,i}^{\text{1st}} = \frac{r_{\text{int,C}_2\text{H}_4,i}}{P_{\text{C}_2\text{H}_6}} \quad (17)$$

Figure 8 shows the Arrhenius dependences (773–873 K for  $\text{C}_2\text{H}_6\text{-O}_2$ , 823–873 K for  $\text{C}_2\text{H}_6\text{-CO}_2$ , and 833–873 K for

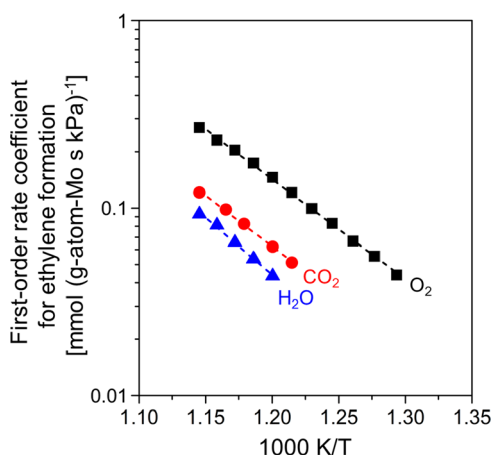


**Figure 8.** Arrhenius dependencies of the first-order, intrinsic rate coefficient ( $k_{\text{int,C}_2\text{H}_4,i}^{\text{1st}}$ , eq 17) for ethylene formation during  $\text{C}_2\text{H}_6\text{-O}_2$  (■),  $\text{C}_2\text{H}_6\text{-CO}_2$  (●), and  $\text{C}_2\text{H}_6\text{-H}_2\text{O}$  (▲) reactions on 13.5 wt %  $\text{MoO}_x/\text{Al}_2\text{O}_3$  catalyst ( $6000 \text{ cm}^3 \text{ h}^{-1} \text{ g}_{\text{cat}}^{-1}$ ).

$\text{C}_2\text{H}_6\text{-H}_2\text{O}$  reaction, respectively) of this rate coefficient for the different catalytic systems, and Table 1 gives the activation barriers. At the initial time, the first-order rate coefficient is higher for the  $\text{C}_2\text{H}_6\text{-O}_2$  than for the  $\text{C}_2\text{H}_6\text{-CO}_2$  reactions, within the accuracy of rate data extrapolation to the zero time. In these reaction systems,  $k_{\text{int,C}_2\text{H}_4,i}^{\text{1st}}$  also equals  $k_{\text{E2}}K_{\text{E1}}$ , as defined

in Scheme 1, and it reflects the elementary rate constant for C–H bond activation of  $\text{C}_2\text{H}_6$  on  $\text{MoO}_x$ . These catalytic systems, however, exhibit similar activation energies (101 vs 105  $\text{kJ mol}^{-1}$ ), because the measured barriers reflect the identical C–H bond activation step. It is plausible that the portion of the highly reactive  $\text{MoO}_x$  sites binds to the  $\text{C}_x\text{H}_y^*$  fragment strongly during the reaction with  $\text{CO}_2$  but not with  $\text{O}_2$  oxidant, even at its first turnover. For the case of the  $\text{C}_2\text{H}_6\text{-H}_2\text{O}$  reaction, the measured activation energy (123  $\text{kJ mol}^{-1}$ ) deviates from the other two cases, because rates are not strictly first-order with respect to  $\text{C}_2\text{H}_6$  pressure, and the first-order rate coefficient  $k_{\text{int,C}_2\text{H}_4,\text{H}_2\text{O}}^{\text{1st}}$  is corrupted by changes in  $\text{OH}^*$  coverages and in the heat of  $\text{H}_2\text{O}$  adsorption ( $K_{\text{H}_2\text{O}}$ ) with temperature (833–873 K).

The kinetic, isotopic, and characterization studies suggest that all reaction systems share the common *Ethane Activation* cycle; the oxidants  $\text{O}_2$  and  $\text{CO}_2$  are involved in catalysis solely through the generation of lattice oxygen atoms required for scavenging the carbonaceous debris and for activating the C–H bond in ethane, thus preventing the over-reduction and carburization of  $\text{MoO}_x$  domains; the oxidant  $\text{H}_2\text{O}$ , however, titrates the lattice oxygen atoms, thus retarding the C–H activation step. The different ethane conversion rates among the various reaction systems reflect the ability of the oxidant in generating reactive oxygen ( $\text{O}^*$ ) species at coverages and reactivities required to scavenge the carbonaceous species. Figure 9 correlates the

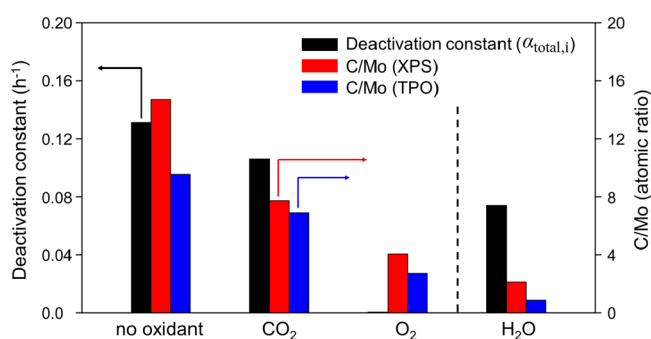


**Figure 9.** Deactivation constants ( $\alpha_{\text{total},i}$ ,  $\text{h}^{-1}$ , eq 9), and carbon contents (atomic C/Mo) determined from both TPO (Figure 5) and XPS (Figure 1) on 13.5 wt %  $\text{MoO}_x/\text{Al}_2\text{O}_3$  catalysts after  $\text{C}_2\text{H}_6$  reactions with  $\text{O}_2$ ,  $\text{H}_2\text{O}$ ,  $\text{CO}_2$ , or without an oxidant for 15 h at 873 K (reaction condition: 5 kPa  $\text{C}_2\text{H}_6$ ; 3.2 kPa  $\text{O}_2$ ,  $\text{CO}_2$ , or  $\text{H}_2\text{O}$ , if added;  $6000 \text{ cm}^3 \text{ h}^{-1} \text{ g}_{\text{cat}}^{-1}$ ).

deactivation constants for ethane turnovers ( $\alpha_{\text{total},i}$ ) and carbon contents (as atomic C/Mo); the latter were determined independently from TPO and XPS studies on spent catalysts after steady-state reactions. Except for the  $\text{C}_2\text{H}_6\text{-H}_2\text{O}$  reaction, there is a direct correlation between the deactivation constants and carbon contents, left by  $\text{C}_2\text{H}_6$  during catalysis in each catalytic system. During catalysis with  $\text{O}_2$ , the rapid, irreversible  $\text{O}_2$  dissociation generates  $\text{O}^*$  effectively, which scavenges carbonaceous intermediates and prevents deactivation. However, these species also react with ethylene product, converting it to  $\text{CO}_x$ , lowering the  $\text{C}_2\text{H}_4$  selectivity. The use of  $\text{CO}_2$  oxidant can retain higher ethylene selectivity than  $\text{O}_2$ , but its activation and concomitant generation of reactive  $\text{O}^*$  species are kinetically restricted, as shown from the RWGS reaction, which is far away from chemical equilibrium. Even if the  $\text{CO}_2$  activation and the related RWGS reaction would attain chemical equilibrium, the oxygen content on the surface is significantly lower than that in the  $\text{C}_2\text{H}_6\text{-O}_2$  ODH reaction, determined to

be  $\sim 10^{22}$  magnitude smaller.  $\text{CO}_2$  removes carbon debris through the kinetically restricted reverse Boudouard reaction ( $\text{CO}_2 + \text{C} (\text{graphite}) \rightarrow 2\text{CO}$ ,  $\Delta H_{298\text{K}}^0 = +172 \text{ kJ mol}^{-1}$ ), in much less effective manner than  $\text{O}_2$  would do. Lastly, the use of  $\text{H}_2\text{O}$  does prevent coke deposition, as shown in Figure 9. In fact, the carbon content is the lowest among all four catalytic systems.  $\text{H}_2\text{O}$  suppresses coke deposition by titrating away the reactive  $\text{O}^*_{\text{lattice}}$  species required for C–H bond activation, converting them to inactive  $\text{OH}^*$ , which neither participates in activating the C–H bond nor assists with the removal of carbonaceous debris.

#### 4. CONCLUSIONS

We have presented an integrated framework for ethane ODH over molybdenum oxide catalysts using different co-oxidants ( $\text{O}_2$ ,  $\text{CO}_2$ , and  $\text{H}_2\text{O}$ ). The proposed framework describes three concomitant, interconnected catalytic cycles: ethane activation, oxidant activation, and carbon removal. The experimental findings presented herewith confirm that the kinetically relevant step (C–H bond activation) remains the same regardless of the identity of the oxidant; the observed difference in rates was rationalized in terms of the chemical identity of the co-oxidant in determining the oxygen chemical potential at the catalytic sites and the ability of the catalysts to sustain continuous scavenging of carbon debris during dehydrogenation. A universal rate expression was synthesized, to incorporate these mechanistic findings, containing two separate terms: one describing the intrinsic  $\text{C}_2\text{H}_6$  activation rates (independent of oxidant identity) and the other one accounting for the time-dependent rate decay (dependent solely on the oxidant ability in scavenging carbon debris). Our findings highlight the critical mechanistic similarities of these diverse ethane (oxy)dehydrogenation systems and provide a different mechanistic perspective, by interpreting a seemingly complex chemistry through a simple mechanistic framework.

#### ■ ASSOCIATED CONTENT

##### SI Supporting Information

The Supporting Information is available free of charge at <https://pubs.acs.org/doi/10.1021/acscatal.0c01073>.

Raman spectrum of 13.5 wt %  $\text{MoO}_x/\text{Al}_2\text{O}_3$  catalyst; catalytic performance on various  $\text{C}_2\text{H}_6$  reactions; deactivation profiles of  $\text{C}_2\text{H}_6\text{--CO}_2$  and  $\text{C}_2\text{H}_6\text{--H}_2\text{O}$  reactions; description for the rate ratio method; rate dependences during various  $\text{C}_2\text{H}_6$  reactions; C 1s XPS spectra of spent 13.5 wt %  $\text{MoO}_x/\text{Al}_2\text{O}_3$  catalysts; experimental details of oxygen vacancy titration studies; derivation of rate expressions (PDF)

#### ■ AUTHOR INFORMATION

##### Corresponding Author

Ya-Huei Cathy Chin – Department of Chemical Engineering and Applied Chemistry, University of Toronto, Toronto M5S 3E5, Ontario, Canada; [orcid.org/0000-0003-4388-0389](https://orcid.org/0000-0003-4388-0389); Phone: (416) 978-8868; Email: [cathy.chin@utoronto.ca](mailto:cathy.chin@utoronto.ca); Fax: (416) 978-8605

##### Authors

Rui Yao – Department of Chemical Engineering and Applied Chemistry, University of Toronto, Toronto M5S 3E5, Ontario, Canada; Key Laboratory of Green Chemical Technology of

Ministry of Education, R&D Center for Petrochemical Technology, Tianjin University, Tianjin 300072, China

José E. Herrera – Department of Chemical and Biochemical Engineering, Western University, London N6A 5B9, Ontario, Canada; [orcid.org/0000-0003-3027-0979](https://orcid.org/0000-0003-3027-0979)

Lihang Chen – Key Laboratory of Green Chemical Technology of Ministry of Education, R&D Center for Petrochemical Technology, Tianjin University, Tianjin 300072, China

Complete contact information is available at: <https://pubs.acs.org/doi/10.1021/acscatal.0c01073>

#### Notes

The authors declare no competing financial interest.

#### ■ ACKNOWLEDGMENTS

This study was supported by the Natural Science and Engineering Research Council of Canada, DCL International Inc., and the Canada Foundation for Innovation. We thank R. Dorakhan for carrying out the  $\text{O}_2$  uptake measurements, and Prof. Song (UWO) for allowing us access to the Raman instrument. R.Y. acknowledges the China Scholarship Council for the financial support.

#### ■ REFERENCES

- (1) Wang, Y.; Tsotsis, T. T.; Jessen, K. Competitive Sorption of Methane/Ethane Mixtures on Shale: Measurements and Modeling. *Ind. Eng. Chem. Res.* **2015**, *54*, 12187–12195.
- (2) Gärtner, C. A.; van Veen, A. C.; Lercher, J. A. Oxidative Dehydrogenation of Ethane: Common Principles and Mechanistic Aspects. *ChemCatChem* **2013**, *5*, 3196–3217.
- (3) Niaei, A.; Towfighi, J.; Sadrameli, S. M.; Karimzadeh, R. The Combined Simulation of Heat Transfer and Pyrolysis Reactions in Industrial Cracking Furnaces. *Appl. Therm. Eng.* **2004**, *24*, 2251–2265.
- (4) He, C.; You, F. Shale Gas Processing Integrated with Ethylene Production: Novel Process Designs, Exergy Analysis, and Techno-Economic Analysis. *Ind. Eng. Chem. Res.* **2014**, *53*, 11442–11459.
- (5) Venegas, J. M.; McDermott, W. P.; Hermans, I. Serendipity in Catalysis Research: Boron-Based Materials for Alkane Oxidative Dehydrogenation. *Acc. Chem. Res.* **2018**, *51*, 2556–2564.
- (6) Cavani, F.; Ballarini, N.; Cericola, A. Oxidative Dehydrogenation of Ethane and Propane: How Far from Commercial Implementation? *Catal. Today* **2007**, *127*, 113–131.
- (7) Doornkamp, C.; Ponc, V. The Universal Character of the Mars and Van Krevelen Mechanism. *J. Mol. Catal. A: Chem.* **2000**, *162*, 19–32.
- (8) Chen, K.; Xie, S.; Bell, A. T.; Iglesia, E. Structure and Properties of Oxidative Dehydrogenation Catalysts Based on  $\text{MoO}_3/\text{Al}_2\text{O}_3$ . *J. Catal.* **2001**, *198*, 232–242.
- (9) Heracleous, E.; Lee, A. F.; Vasalos, I. A.; Lemonidou, A. A. Surface Properties and Reactivity of  $\text{Al}_2\text{O}_3$ -Supported  $\text{MoO}_3$  Catalysts in Ethane Oxidative Dehydrogenation. *Catal. Lett.* **2003**, *88*, 47–53.
- (10) Argyle, M. D.; Chen, K.; Bell, A. T.; Iglesia, E. Effect of Catalyst Structure on Oxidative Dehydrogenation of Ethane and Propane on Alumina-Supported Vanadia. *J. Catal.* **2002**, *208*, 139–149.
- (11) Chen, K.; Xie, S.; Iglesia, E.; Bell, A. T. Structure and Properties of Zirconia-Supported Molybdenum Oxide Catalysts for Oxidative Dehydrogenation of Propane. *J. Catal.* **2000**, *189*, 421–430.
- (12) Chen, K.; Xie, S.; Bell, A. T.; Iglesia, E. Alkali Effects on Molybdenum Oxide Catalysts for the Oxidative Dehydrogenation of Propane. *J. Catal.* **2000**, *195*, 244–252.
- (13) Porosoff, M. D.; Myint, M. N. Z.; Kattel, S.; Xie, Z.; Gomez, E.; Liu, P.; Chen, J. G. Identifying Different Types of Catalysts for  $\text{CO}_2$  Reduction by Ethane through Dry Reforming and Oxidative Dehydrogenation. *Angew. Chem., Int. Ed.* **2015**, *54*, 15501–15505.
- (14) Yao, S.; Yan, B.; Jiang, Z.; Liu, Z.; Wu, Q.; Lee, J. H.; Chen, J. G. Combining  $\text{CO}_2$  Reduction with Ethane Oxidative Dehydrogenation

by Oxygen-Modification of Molybdenum Carbide. *ACS Catal.* **2018**, *8*, 5374–5381.

(15) Myint, M.; Yan, B.; Wan, J.; Zhao, S.; Chen, J. G. Reforming and Oxidative Dehydrogenation of Ethane with CO<sub>2</sub> as a Soft Oxidant over Bimetallic Catalysts. *J. Catal.* **2016**, *343*, 168–177.

(16) Shen, A.-L.; Weng, Y.-C.; Chou, T.-C. Effect of the Analytic Regions on the Quality Trend of Diamond-Like/Graphitic Carbon Ratios in Raman Spectra. *Z. Naturforsch., B: J. Chem. Sci.* **2010**, *65*, 67–71.

(17) Oshikawa, K.; Nagai, M.; Omi, S. Characterization of Molybdenum Carbides for Methane Reforming by TPR, XRD, and XPS. *J. Phys. Chem. B* **2001**, *105*, 9124–9131.

(18) Wang, H.; Liu, S.; Smith, K. J. Synthesis and Hydrodeoxygenation Activity of Carbon Supported Molybdenum Carbide and Oxycarbide Catalysts. *Energy Fuels* **2016**, *30*, 6039–6049.

(19) Nobbs, J. H. Kubelka–Munk Theory and the Prediction of Reflectance. *Rev. Prog. Color. Relat. Top.* **1985**, *15*, 66–75.

(20) Davis, E. A.; Mott, N. F. Conduction in Non-Crystalline Systems V. Conductivity, Optical Absorption and Photoconductivity in Amorphous Semiconductors. *Philos. Mag.* **1970**, *22*, 0903–0922.

(21) Carrero, C. A.; Schloegl, R.; Wachs, I. E.; Schomaecker, R. Critical Literature Review of the Kinetics for the Oxidative Dehydrogenation of Propane over Well-Defined Supported Vanadium Oxide Catalysts. *ACS Catal.* **2014**, *4*, 3357–3380.

(22) Wachs, I. E.; Roberts, C. A. Monitoring Surface Metal Oxide Catalytic Active Sites with Raman Spectroscopy. *Chem. Soc. Rev.* **2010**, *39*, 5002–5017.

(23) Spevack, P. A.; McIntyre, N. S. A Raman and XPS Investigation of Supported Molybdenum Oxide Thin Films. 1. Calcination and Reduction Studies. *J. Phys. Chem.* **1993**, *97*, 11020–11030.

(24) Tian, H.; Roberts, C. A.; Wachs, I. E. Molecular Structural Determination of Molybdena in Different Environments: Aqueous Solutions, Bulk Mixed Oxides, and Supported MoO<sub>3</sub> Catalysts. *J. Phys. Chem. C* **2010**, *114*, 14110–14120.

(25) Chua, Y. T.; Stair, P. C.; Wachs, I. E. A Comparison of Ultraviolet and Visible Raman Spectra of Supported Metal Oxide Catalysts. *J. Phys. Chem. B* **2001**, *105*, 8600–8606.

(26) Chakrabarti, A.; Wachs, I. E. Molecular Structure–Reactivity Relationships for Olefin Metathesis by Al<sub>2</sub>O<sub>3</sub>-Supported Surface MoO<sub>x</sub> Sites. *ACS Catal.* **2018**, *8*, 949–959.

(27) Mestl, G.; Srinivasan, T. K. K. Raman Spectroscopy of Monolayer-Type Catalysts: Supported Molybdenum Oxides. *Catal. Rev.: Sci. Eng.* **1998**, *40*, 451–570.

(28) Thielemann, J. P.; Ressler, T.; Walter, A.; Tzolova-Müller, G.; Hess, C. Structure of Molybdenum Oxide Supported on Silica SBA-15 Studied by Raman, UV–Vis and X-ray Absorption Spectroscopy. *Appl. Catal., A* **2011**, *399*, 28–34.

(29) Phillips, D. C.; Sawhill, S. J.; Self, R.; Bussell, M. E. Synthesis, Characterization, and Hydrodesulfurization Properties of Silica-Supported Molybdenum Phosphide Catalysts. *J. Catal.* **2002**, *207*, 266–273.

(30) Datta, R. S.; Haque, F.; Mohiuddin, M.; Carey, B. J.; Syed, N.; Zavabeti, A.; Zhang, B.; Khan, H.; Berean, K. J.; Ou, J. Z.; Mahmood, N.; Daeneke, T.; Kalantar-zadeh, K. Highly Active Two Dimensional  $\alpha$ -MoO<sub>3-x</sub> for the Electrocatalytic Hydrogen Evolution Reaction. *J. Mater. Chem. A* **2017**, *5*, 24223–24231.

(31) Nag, N. K. A Comparative Study on the Dispersion and Carrier-Catalyst Interaction of Molybdenum Oxides Supported on Various Oxides by Electron Spectroscopy for Chemical Analysis. *J. Phys. Chem.* **1987**, *91*, 2324–2327.

(32) Zingg, D. S.; Makovsky, L. E.; Tischer, R. E.; Brown, F. R.; Hercules, D. M. A Surface Spectroscopic Study of Molybdenum-Alumina Catalysts Using X-ray Photoelectron, Ion-Scattering, and Raman Spectroscopies. *J. Phys. Chem.* **1980**, *84*, 2898–2906.

(33) Meyer, J.; Kidambi, P. R.; Bayer, B. C.; Weijtens, C.; Kuhn, A.; Centeno, A.; Pesquera, A.; Zurutuza, A.; Robertson, J.; Hofmann, S. Metal Oxide Induced Charge Transfer Doping and Band Alignment of Graphene Electrodes for Efficient Organic Light Emitting Diodes. *Sci. Rep.* **2015**, *4*, 5380.

(34) Head, A. R.; Tsyshevsky, R.; Trotochaud, L.; Yu, Y.; Kyhl, L.; Karşloğlu, O.; Kuklja, M. M.; Bluhm, H. Adsorption of Dimethyl Methylphosphonate on MoO<sub>3</sub>: The Role of Oxygen Vacancies. *J. Phys. Chem. C* **2016**, *120*, 29077–29088.

(35) Weber, R. S. Effect of Local Structure on the UV-Visible Absorption Edges of Molybdenum Oxide Clusters and Supported Molybdenum Oxides. *J. Catal.* **1995**, *151*, 470–474.

(36) Dieterle, M.; Weinberg, G.; Mestl, G. Raman Spectroscopy of Molybdenum Oxides Part I. Structural Characterization of Oxygen Defects in MoO<sub>3-x</sub> by DR UV/Vis, Raman Spectroscopy and X-ray Diffraction. *Phys. Chem. Chem. Phys.* **2002**, *4*, 812–821.

(37) Xiong, G.; Feng, Z.; Li, J.; Yang, Q.; Ying, P.; Xin, Q.; Li, C. UV Resonance Raman Spectroscopic Studies on the Genesis of Highly Dispersed Surface Molybdate Species on  $\gamma$ -Alumina. *J. Phys. Chem. B* **2000**, *104*, 3581–3588.

(38) Barton, D. G.; Shtein, M.; Wilson, R. D.; Soled, S. L.; Iglesia, E. Structure and Electronic Properties of Solid Acids Based on Tungsten Oxide Nanostructures. *J. Phys. Chem. B* **1999**, *103*, 630–640.

(39) Weckhuysen, B. M.; Schoonheydt, R. A. Recent Progress in Diffuse Reflectance Spectroscopy of Supported Metal Oxide Catalysts. *Catal. Today* **1999**, *49*, 441–451.

(40) Wilson, R. D.; Barton, D. G.; Baertsch, C. D.; Iglesia, E. Reaction and Deactivation Pathways in Xylene Isomerization on Zirconia Modified by Tungsten Oxide. *J. Catal.* **2000**, *194*, 175–187.

(41) Abdelrahman, O. A.; Luo, H. Y.; Heyden, A.; Román-Leshkov, Y.; Bond, J. Q. Toward Rational Design of Stable, Supported Metal Catalysts for Aqueous-Phase Processing: Insights from the Hydrogenation of Levulinic Acid. *J. Catal.* **2015**, *329*, 10–21.

(42) Bleken, F. L.; Janssens, T. V. W.; Svelle, S.; Olsbye, U. Product Yield in Methanol Conversion over ZSM-5 Is Predominantly Independent of Coke Content. *Microporous Mesoporous Mater.* **2012**, *164*, 190–198.

(43) Foley, B. L.; Johnson, B. A.; Bhan, A. A Method for Assessing Catalyst Deactivation: A Case Study on Methanol-to-Hydrocarbons Conversion. *ACS Catal.* **2019**, *9*, 7065–7072.

(44) Prasomsri, T.; Shetty, M.; Murugappan, K.; Román-Leshkov, Y. Insights into the Catalytic Activity and Surface Modification of MoO<sub>3</sub> During the Hydrodeoxygenation of Lignin-Derived Model Compounds into Aromatic Hydrocarbons under Low Hydrogen Pressures. *Energy Environ. Sci.* **2014**, *7*, 2660–2669.

(45) Li, Y.; Fan, Y.; He, J.; Xu, B.; Yang, H.; Miao, J.; Chen, Y. Selective Liquid Hydrogenation of Long Chain Linear Alkadienes on Molybdenum Nitride and Carbide Modified by Oxygen. *Chem. Eng. J.* **2004**, *99*, 213–218.

(46) Murugappan, K.; Anderson, E. M.; Teschner, D.; Jones, T. E.; Skorupska, K.; Román-Leshkov, Y. Operando NAP-XPS Unveils Differences in MoO<sub>3</sub> and Mo<sub>2</sub>C During Hydrodeoxygenation. *Nat. Catal.* **2018**, *1*, 960–967.

(47) Ji, Z.; Lv, H.; Pan, X.; Bao, X. Enhanced Ethylene Selectivity and Stability of Mo/ZSM5 Upon Modification with Phosphorus in Ethane Dehydrogenation. *J. Catal.* **2018**, *361*, 94–104.

(48) Qiu, J.; Yang, Z.; Li, Q.; Li, Y.; Wu, X.; Qi, C.; Qiao, Q. Formation of N-Doped Molybdenum Carbide Confined in Hierarchical and Hollow Carbon Nitride Microspheres with Enhanced Sodium Storage Properties. *J. Mater. Chem. A* **2016**, *4*, 13296–13306.

(49) Lee, W.-S.; Wang, Z.; Wu, R. J.; Bhan, A. Selective Vapor-Phase Hydrodeoxygenation of Anisole to Benzene on Molybdenum Carbide Catalysts. *J. Catal.* **2014**, *319*, 44–53.

(50) Xiao, T.-C.; York, A. P. E.; Al-Megren, H.; Williams, C. V.; Wang, H.-T.; Green, M. L. H. Preparation and Characterisation of Bimetallic Cobalt and Molybdenum Carbides. *J. Catal.* **2001**, *202*, 100–109.

(51) Xiao, T.-C.; York, A. P. E.; Williams, C. V.; Al-Megren, H.; Hanif, A.; Zhou, X.-Y.; Green, M. L. H. Preparation of Molybdenum Carbides Using Butane and Their Catalytic Performance. *Chem. Mater.* **2000**, *12*, 3896–3905.

(52) Xiang, X.; Zhang, L.; Hima, H. I.; Li, F.; Evans, D. G. Co-Based Catalysts from Co/Fe/Al Layered Double Hydroxides for Preparation of Carbon Nanotubes. *Appl. Clay Sci.* **2009**, *42*, 405–409.

(53) Ma, D.; Wang, D.; Su, L.; Shu, Y.; Xu, Y.; Bao, X. Carbonaceous Deposition on Mo/HMCM-22 Catalysts for Methane Aromatization: A TP Technique Investigation. *J. Catal.* **2002**, *208*, 260–269.

(54) Shetty, M.; Murugappan, K.; Prasomsri, T.; Green, W. H.; Román-Leshkov, Y. Reactivity and Stability Investigation of Supported Molybdenum Oxide Catalysts for the Hydrodeoxygenation (HDO) of M-Cresol. *J. Catal.* **2015**, *331*, 86–97.

(55) Chen, K.; Bell, A. T.; Iglesia, E. Kinetics and Mechanism of Oxidative Dehydrogenation of Propane on Vanadium, Molybdenum, and Tungsten Oxides. *J. Phys. Chem. B* **2000**, *104*, 1292–1299.

(56) Argyle, M. D.; Chen, K.; Bell, A. T.; Iglesia, E. Ethane Oxidative Dehydrogenation Pathways on Vanadium Oxide Catalysts. *J. Phys. Chem. B* **2002**, *106*, 5421–5427.

(57) Chen, K.; Khodakov, A.; Yang, J.; Bell, A. T.; Iglesia, E. Isotopic Tracer and Kinetic Studies of Oxidative Dehydrogenation Pathways on Vanadium Oxide Catalysts. *J. Catal.* **1999**, *186*, 325–333.

(58) Annamalai, L.; Liu, Y.; Ezenwa, S.; Dang, Y.; Suib, S. L.; Deshlahra, P. Influence of Tight Confinement on Selective Oxidative Dehydrogenation of Ethane on MoVTenb Mixed Oxides. *ACS Catal.* **2018**, *8*, 7051–7067.

(59) Chen, K.; Iglesia, E.; Bell, A. T. Isotopic Tracer Studies of Reaction Pathways for Propane Oxidative Dehydrogenation on Molybdenum Oxide Catalysts. *J. Phys. Chem. B* **2001**, *105*, 646–653.

(60) Fu, G.; Xu, X.; Lu, X.; Wan, H. Mechanisms of Initial Propane Activation on Molybdenum Oxides: A Density Functional Theory Study. *J. Phys. Chem. B* **2005**, *109*, 6416–6421.

(61) Fu, H.; Liu, Z.-P.; Li, Z.-H.; Wang, W.-N.; Fan, K.-N. Periodic Density Functional Theory Study of Propane Oxidative Dehydrogenation over V<sub>2</sub>O<sub>5</sub>(001) Surface. *J. Am. Chem. Soc.* **2006**, *128*, 11114–11123.

(62) Dai, G.-L.; Li, Z.-H.; Lu, J.; Wang, W.-N.; Fan, K.-N. Deep Oxidations in the Oxidative Dehydrogenation Reaction of Propane over V<sub>2</sub>O<sub>5</sub>(001): Periodic Density Functional Theory Study. *J. Phys. Chem. C* **2012**, *116*, 807–817.

(63) Gilardoni, F.; Bell, A. T.; Chakraborty, A.; Boulet, P. Density Functional Theory Calculations of the Oxidative Dehydrogenation of Propane on the (010) Surface of V<sub>2</sub>O<sub>5</sub>. *J. Phys. Chem. B* **2000**, *104*, 12250–12255.

(64) Zhao, Z.-J.; Wu, T.; Xiong, C.; Sun, G.; Mu, R.; Zeng, L.; Gong, J. Hydroxyl-Mediated Non-Oxidative Propane Dehydrogenation over VO<sub>x</sub>/γ-Al<sub>2</sub>O<sub>3</sub> Catalysts with Improved Stability. *Angew. Chem., Int. Ed.* **2018**, *57*, 6791–6795.

(65) Choksi, T.; Greeley, J. Partial Oxidation of Methanol on MoO<sub>3</sub>(010): A DFT and Microkinetic Study. *ACS Catal.* **2016**, *6*, 7260–7277.

(66) Oyama, S. T.; Middlebrook, A. M.; Somorjai, G. A. Kinetics of Ethane Oxidation on Vanadium Oxide. *J. Phys. Chem.* **1990**, *94*, 5029–5033.

(67) Wei, J.; Iglesia, E. Mechanism and Site Requirements for Activation and Chemical Conversion of Methane on Supported Pt Clusters and Turnover Rate Comparisons among Noble Metals. *J. Phys. Chem. B* **2004**, *108*, 4094–4103.

(68) Wei, J.; Iglesia, E. Isotopic and Kinetic Assessment of the Mechanism of Reactions of CH<sub>4</sub> with CO<sub>2</sub> or H<sub>2</sub>O to Form Synthesis Gas and Carbon on Nickel Catalysts. *J. Catal.* **2004**, *224*, 370–383.

(69) Tu, W.; Ghossoub, M.; Singh, C. V.; Chin, Y.-H. C. Consequences of Surface Oxophilicity of Ni, Ni-Co, and Co Clusters on Methane Activation. *J. Am. Chem. Soc.* **2017**, *139*, 6928–6945.

(70) Wei, J.; Iglesia, E. Reaction Pathways and Site Requirements for the Activation and Chemical Conversion of Methane on Ru-Based Catalysts. *J. Phys. Chem. B* **2004**, *108*, 7253–7262.